

Novel algorithms for efficiently accumulating, analysing and visualising full-waveform LiDAR in a volumetric representation with applications to forestry

submitted by

Milto Miltiadou

for the degree of Doctor of Engineering

of the

University of Bath

Centre for Digital Entertainment

and of the

Plymouth Marine Laboratory

NERC Airborne Research Facility

December 2016

COPYRIGHT

Attention is drawn to the fact that copyright of this thesis rests with its author. This copy of the thesis has been supplied on the condition that anyone who consults it is understood to recognise that its copyright rests with its author and that no quotation from the thesis and no information derived from it may be published without the prior written consent of the author.

This thesis may be made available for consultation within the University Library and may be photocopied or lent to other libraries for the purposes of consultation.

Signature of Author.....

Milto Miltiadou

Abstract

no more than 300 words

NOTES:

Blue colour: additions according to Neill's feedback,

Purple colour: addition/corrections according to Mike's comments

Red colour: notes

Gray colour: text that is going to be modified

To be added on top

Abstract

This study focuses on enhancing the visualisations and classifications of forested areas using coincident full-waveform (fw) LiDAR data and hyperspectral images. The ultimate aim is use both datasets to derive information about forests and show the results on a 3D virtual, interactive environment. Influenced by Persson et al (2005), voxelisation is an integral part of this research. The intensity profile of each full-waveform pulse is accumulated into a voxel array, building up a 3D density volume. The correlation between multiple pulses into a voxel representation produces a more accurate representation, which confers greater noise resistance and it further opens up possibilities of vertical interpretation of the data. The 3D density volume is then aligned with the hyperspectral images using a 2D grid similar to Warren et al (2014) and both datasets are used in visualisations and classifications.

Previous work in visualising fw LiDAR has used transparent objects and point clouds, while the output of this system is a coloured 3D-polygon representation, showing well-separated structures such as individual trees and greenhouses. The 3D density volume, generated from the fw LiDAR data, is polygonised using functional representation of object (FReps) and the marching cubes algorithm (Pasko and Savchenko, 1994) (Lorensen and Cline, 1987). Further, an optimisation algorithm is introduced that uses integral volumes (Crow, 1984) to speed up the process of polygonising the volume. This optimisation approach not only works on non-manifold object, but also a speed up of up to 51% was achieved. The polygon representation is also textured by projecting the hyperspectral images into the mesh. In addition, the output is suitable for direct rendering with commodity 3D-accelerated hardware, allowing smooth visualisation.

In future work, the effects of combining both hyperspectral imagery and fw LiDAR in classifications and visualisations are examined. At first, two pixel wise classifiers, a support vector machine and a Bayesian probabilistic model, will be used for testing the effects of the combination in generating tree coverage maps. Higher accuracy classification results are expected when metrics from both datasets are used together. Regarding the visualisations, the differences of applying surface reconstruction versus direct volumetric rendering will be discussed and an ordered tree structure with integral sums of the node values will be used for speeding up the ray-tracing of direct volumetric rendering and improving memory management of aforementioned optimisation algorithm with integral volumes. Further, deferred rendering is suggested for testing the visual human perception of projecting multiple bands of the hyperspectral images on the FW LiDAR

polygon representations. At the end of this project the combination of the datasets will be used along with the watershed algorithm for tree segmentation, which is useful for measuring the stem density of a forest and for tree species classifications.

from EDE:

Firstly, a new and fast way of aligning the FW LiDAR with Remotely Sensed Images has been developed in DASOS and by generating tree coverage maps it was shown that the combination of those datasets confers better remote survey results. This work was presented at the 36th ISRSE International Conference.

Secondly, automated detection of dead trees in native Australian forests has a significant role in protecting animals, which live in those trees and are close to extinction. DASOS allow the generation of 3D signatures characterising dead trees. A comparison between the discrete and FW LiDAR is performed to demonstrate the increased survey accuracy obtained when the FW LiDAR are used.

Finally, the last application is for improving visualisations for foresters. Foresters have a great knowledge about forests and can derive a wealth of information directly from visualisations of the remotely sensed data. This reduces the travelling time and cost of getting into the forests. This research optimises visualisations by using the new FW LiDAR representations and a speed of up to 51% has been achieved.

FW LiDAR has great potentials in forestry and this research has already started to have an impact in the FW LiDAR community by making those huge datasets easier to handle. DASOS is now used at Interpine Group Ltd, a world leading Forestry Company in New Zealand and it has been tested from a PhD student at Bournemouth University who looks into estimating bird distribution in the New Forest. In the future, it is expected that DASOS will be widely used in remote forest surveys (i.e. estimating the commercial value of a forest and detecting infected trees at early stages for treatment).

Acknowledgements

Above all, I would like to express my great gratitude to my industrial supervisors Dr. Michael Grant who had supported me continuously during my research and gave me the freedom to create a project of my own interest.

Then, I would like to thanks Dr. Matthew Brown, who helped me during my first years of my studies by giving me valuable and informative feedback. He was always there to keep me working on the right track.

Equally important is my current supervisor Dr. Neil D.F. Campbell and he is not to be missed from the acknowledgements.

Furthermore, special thanks are given to Dr. Mark Warren, Dr. Darren Cosker, MSc Susana Gonzalez Aracil and Dr. Ross Hill who occasionally advised me during my studies.

It further worth giving credits to my data providers, the Natural Environment Research Council's Airborne Research Facility (NERC ARF) and Interpine Group Ltd.

Last but not least, I am extremely grateful to my funding organisations, the Centre for Digital Entertainment and Plymouth Marine Laboratory, who supported financially and consequently made this research possible.

Abbreviations and Glossary

AGC	Automatic Gain Controller
ALS	Airborne Laser Scanning
APL	Airborne Processing Library
ARF	Airborne Research Facility
CG	Computer Graphics
CUDA	parallel computing platform available on nvidia graphic cards (=forest in Greek), the open source software implemented for managing FW LiDAR data
DEM	Digital Elevation Model
DTM	Digital Terrain Model (DTM)
FW	Full-Waveform
GB	Gigabyte
GPU	Graphics Processing Unit
LiDAR	Light Detection And Ranging
NASA	National Aeronautics and Space Administration
NDVI	Normalised Difference Vegetation Index
NERC	Natural Environment Research Council
NIR	Near-Infrared Region of the electromagnetic spectrum
TB	Terabyte
VIS	VIvisual Spectrum
VLR	Variable Length Records
WPDF	Waveform Packet Descriptor Format
UK	United Kingdom

Publications

DASOS-User Guide, M. Miltiadou, N.D.F Campbell, M. Brown, S.C. Aracil, M.A. Warren, D. Clewley, D.Cosker, and M. Grant, Full-waveform LiDAR workshop at Interpine Group Ltd, Rotorua NZ, 2016

Alignment of Hyperspectral Imagery and Full-Waveform LiDAR data for visualisation and classification purposes, M. Miltiadou, M. A. Warren, M. Grant, and M. Brown, *The International Archives of Photogrammetry, Remote Sensing and Spatial Information Sciences*, vol. 40, no. 7, p. 1257, 2015.

Reconstruction of a 3D Polygon Representation from Full-Wavefrom LiDAR data, M. Miltiadou, M. Grant, M. Brown, M. Warren, and E. Carolan, *RSPSoc Annual Conference, New Sensors for a Changing World*, 2014.

Awards

EDE and Ravenscroft Prize - Finalist: Selected as one of the five finalists for this is a prestigious prize that recognises the work of best postgraduate researchers.

Student Poster Competition at Silvilaser.

Conference Presentations

ForestSAT Conference, Santiago, Chile, 2016 - Oral and Poster Presentation

Computer Graphics & Visual Computing (CGVC), Bournemouth, United Kingdom, 2016 - Poster Presentation

Silvilaser, La Grant Motte, France, 2015 - Oral Presentation

International Symposium of Remote Sensing of the Environment (ISRSE), 2015 - Oral Presentation

RSPSoc Conference, New Sensors for a Changing world, Aberystwyth, United Kingdom, 2014 - Oral Presentation

Contents

Abstract	i
Acknowledgements	iii
Abbreviations and Glossary	iv
Publications	v
Awards	v
Conference Presentations	v
List of Figures	viii
1 Introduction	1
1.1 Forest Monitoring: Importance and Applications	1
1.2 Background Information about Remote Sensing and Airborne Laser Scanning Systems	2
2 Acquire Data	3
2.1 Airborne LiDAR systems: An in-depth Explanation	5
2.2 Brief Description of the LAS1.3 File Format	6
2.3 Leica Vs Trimble Instruments: Limitations, Differences and Advantages	6
2.4 Hyperspectral Imagery	8
3 Overview of Thesis	11
4 The open source software DASOS and the Voxelisation Approach	12
5 Surface Reconstruction from Voxelised FW LiDAR Data	13
5.1 Introduction	13
5.2 Rendering Approaches of Volumetric Data	13
5.3 Algebraic Definition of the Volume	14
5.4 Surface Reconstruction with the Marching Cubes Algorithm	15
5.5 Results	16

6 Optimisation Attempts for the Surface Reconstruction	22
6.1 Problem and Challenges	22
6.2 Related work	23
6.3 Overview	25
6.4 The Optimisation Methods	26
6.5 Integral Volumes	26
6.6 Octree Max and Min <i>**Everything from here is new :)</i>	31
6.7 Integral Tree	34
6.8 Results and Discussion	36
7 Alignment with Hyperspectral Imagery	40
8 Classifications using 3D Prior Models	41
9 Comparison with Discrete Data	44
10 Overall Results	46
11 Conclusions	47
11.1 Contributions	48
Bibliography	48
12 Appendices	55
12.1 Birds and Mammals Catalogue	55

List of Figures

2-1	Data and Instruments	4
2-2	Airborne Laser Scanning System	4
2-3	LAS1.3 File Format	7
2-4	Hyperpsectral Cube	10
5-1	Marching Cubes Sampling	17
5-2	Animation Packages	18
5-3	Various Flightlines Visualisation	18
5-4	Selecting Region of Interest	19
5-5	Polygonisation Parameters	20
5-6	3D printing	21
6-1	Integral Image	27
6-2	Comparison between including and ignoring neighbourouing voxels; holes appears when ignored.	29
6-3	This diagram depicts the parameters used for finding neighbouring voxels.	33
6-4	Ordering of tree elements	34
6-5	Illustration of how to save the values of an Integral Quad Tree into the 1D-array, in order to preserve the condition of Integral Trees	35
6-6	Example of Integral Binary Tree	35

Chapter 1

Introduction

1.1 Forest Monitoring: Importance and Applications

Forest monitoring involves checking and observing the changes in the structure of the forests and their foliage over the years. It has a significant value in both sustainable and commercial forests, because it contributes into managing biodiversity, maintaining forest health and optimising wood trade procedures as explained below:

- **Biodiversity** plays a substantial role in ecosystem resilience [1] while various human activities affect biological communities by altering their composition and leading species to extinction [2]. For example, in Australian native forests many arboreal mammals and birds rely on hollow trees for shelters [3]. Hollow trees are trees that have hollows, which are semi-enclosed cavity on trunks and branches. They are formed by natural forces, like bacteria, fungi and insects and it takes hundreds of years to become suitable for animal/bird shelters. Unfortunately recent studies shown that there us likely to be a shortage of hollows available for colonisation in the near future [4] [5]. Therefore monitoring and protecting hollow trees have a positive impact in preserving biodiversity.
- **Forest Health:** Protecting vegetation from pests and diseases. An example of pests are the Brushtail Possums, which were initially brought to New Zealand for fur trade, but they have escaped and become a threat to native forests and vegetation [6]. In addition, anthropogenic factors have a negative impact to nature. For instance, acid rain is responsible for the freezing decease at red bruces because it reduces the membrane-associated calcium, which is important for tolerating cold [7]. Those changes in nature need to be monitor in order to preserve a healthy and resilience ecosystem.

- **Wood Trade:** Measuring stem volume and basal areas of trees contributes to forest planning and management [8]. For example, measuring stocking and wood quality would help into estimating the cost of harvesting the trees in relation to the stocking [9].

Traditionally, forest monitoring involves field work such as travelling into the area of interest and taking manual measurements. Regarding the need to monitor hollows, tree climbing with ladders and ropes gives very accurate results but it's dangerous, expensive, time consuming, and cannot easily scale into large forested areas [10] [11]. Therefore, automated ways of monitoring forests are essential and this is why Remote Sensing has a significantly positive impact in forestry.

1.2 Background Information about Remote Sensing and Airborne Laser Scanning Systems

Chapter 2

Acquire Data

The aim of this section is to give a practical and scientific insight into the acquisition of data, because a good knowledge of these methods and their limitations is essential for understanding the related research undertaken. The relations between the two main datasets used in this project are depicted on Figure 2-1 and briefly explained here:

- The **New Forest dataset** from the UK was provided by the Natural Environment Research Council's Airborne Research Facility (NERC ARF). Measurements were collected simultaneously a Leica ALS50-II LiDAR and AISA Eagle/Hawk hyperspectral radiometers on the 8th of April in 2010. It contains Discrete LiDAR, FW LiDAR and hyperspectral images.
- The **RedGum dataset** was acquired in Australia using a Trimble AX60 integrated LiDAR/Camera instrument over the time period from the 6th of March in 2015 until the 31st of March in 2015. It was provided by the RPS Australia East Pty Ltd. Only the FW LiDAR data are used here.

The ALS data are explained first, because they are the main focus of this research, and hyperspectral imagery is towards the end of the chapter. In Section 2.1, an in-depth description of ALS systems and the differences between discrete and FW LiDAR data is given. Section 2.2 briefly discusses the binary file format of the acquired LiDAR data and Section 2.3 is a discussion on the limitations, the differences and the advantages of two LiDAR instruments; the Leica and Trimble. The essential information about the hyperspectral imagery, which is only associated with the New Forest dataset, is then covered in Section 2.4.

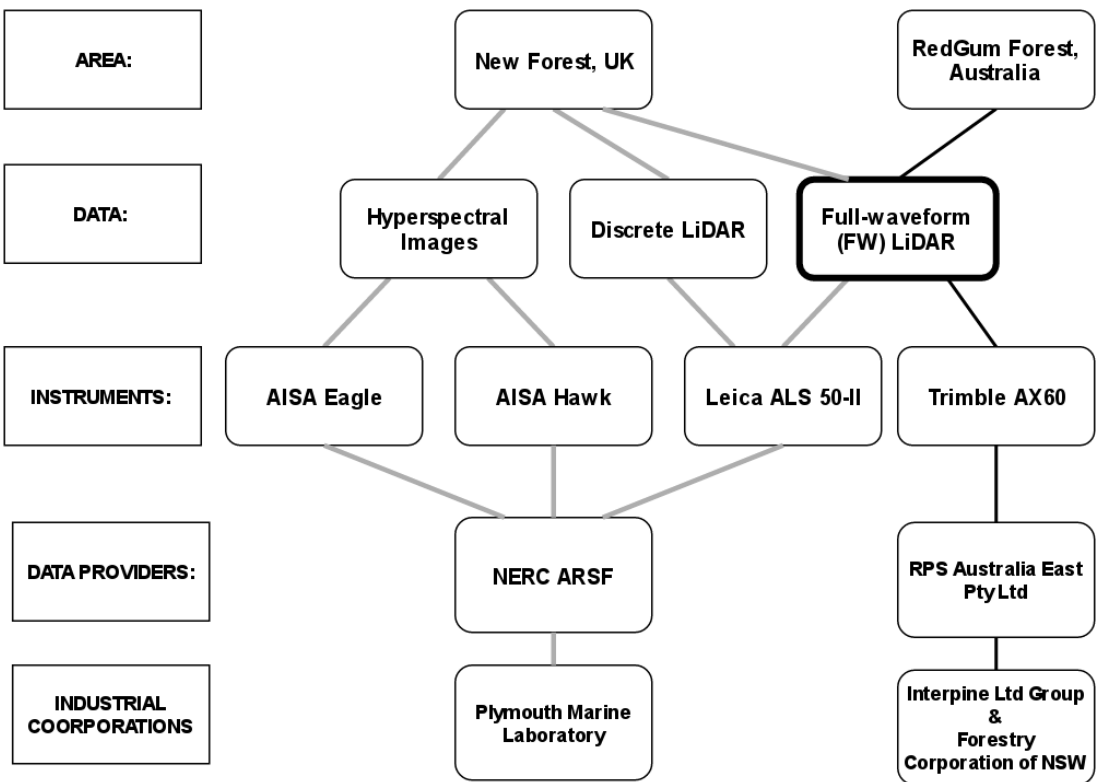


Figure 2-1: Data and Instruments

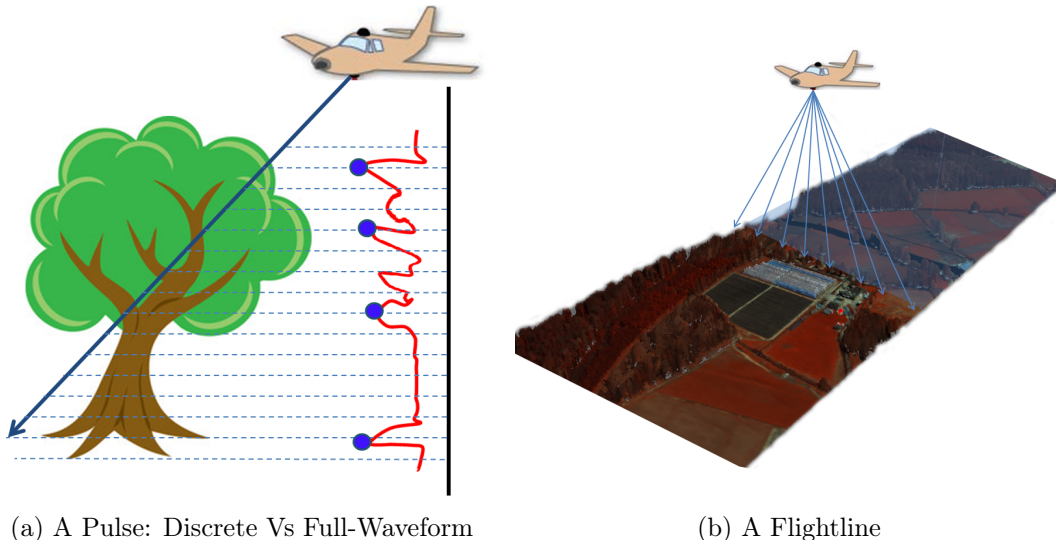


Figure 2-2: Airborne Laser Scanning System

2.1 Airborne LiDAR systems: An in-depth Explanation

The ALS systems emit laser pulses from sensor mounted in a plane and collects information from the time-of-flight and the returned laser intensity. By the time the pulse has travelled the approximately 1-3km from the aircraft to the ground, it is roughly 20cm in width due to beam divergence. When the pulse hits an object (e.g. the forest canopy), then some of it reflects back while the rest penetrates through holes between leaves and branches. The laser pulse continues to hit structures, scattering and partially returning to the sensor until it reaches a solid barrier such as the ground and is fully blocked from further progress. The LiDAR systems record information from the backscattered laser pulse, measuring its round trip time and the returned intensity.

As mentioned at Section 1.2, there are two types of LiDAR data, discrete and FW. The discrete LiDAR observes the returned intensity signals and identifies and [records a few peak intensity returns of the signal](#), while the FW LiDAR system digitises and stores the entire backscattered signal into equally spaced time intervals (Figure 2-2a). The delivered data for the discrete LiDAR is a set of hit points ("returns"), which are associated with laser intensities. The world position of every return is calculated by measuring the round trip time of the laser return, giving a distance from the sensor, which is combined with the precisely known position and orientation of the aircraft/sensor (from GPS, an inertial measurement unit and precise shot direction of the laser pulse). The waveform recordings are triggered by and attached to first returns of discrete LiDAR data (to avoid sampling the uninteresting time period while the pulse travels through the atmosphere) and they are a list of intensities that correspond to the laser intensity returned over time. There is also an offset vector which defines the distance and direction between each wave sample (effectively a compression mechanism, by avoid recording the world position of every sample, replacing it with the location of the first return and this vector).

As shown in Figure 2-2b, the pulses are scanned back and forth across the landscape below (by a rotating mirror) as the plane travels forward. The scanned data has a limited maximum width according to the flight height and the field of view scan angle. During processing the track of the plane is divided into easier-to-handle pieces (flightlines) and saved into separate binary files. In this project the LAS1.3 file format is used for both datasets.

2.2 Brief Description of the LAS1.3 File Format

There are a few LiDAR file formats but the LAS1.3 was the first format to contain FW data and it is the one used to store the data for both New Forest and RedGum datasets. According to the LAS1.3 file specifications [18], a .LAS file contains information about both discrete and FW LiDAR data, with the waveform packets attached to discrete returns and saved either internally at the end of the .LAS file or externally in a .WVS file.

As shown at (Figure 2-3) the .LAS file is divided into four sections and a brief explanation of each section is given here:

1. The **Header** contains general information about the entire flightline. For example, it includes the maximum scan angle used during the flight, whether the waveform packets are recorded internally or externally and the number of **Variable Length Records** (VLR).
2. Regarding the **VLR**, which contain arbitrary "extension" data blocks, the most important information given is the waveform packet descriptors that contain essential information on how to read the waveform packets (i.e. an ID, the number of wave samples and the size of each intensity in bits).
3. The **Point Data Records** are the discrete points and the waveforms are associated with first return discrete points. Each Point Data Record has a spatial location, an intensity and optionally a pointer to a waveform packet as well as the ID of the corresponding waveform packet descriptor.
4. The waveform packets is a list of intensities and they are either saved internally into the **Extended Variable Length Records** section of the .LAS file or inside an external .WVS file. Starting from the associated first return point, the spatial locations of the waveform packet (wave sample intensity) are calculated by adding an offset defined in the associated Point Data Record.

2.3 Leica Vs Trimble Instruments: Limitations, Differences and Advantages

As shown in Figure 2-1, the Leica ALS 50-II instrument was used to capture the LiDAR data of New Forest dataset and the Trimble AX60 for collecting the RedGum Forest FW LiDAR data. It is therefore important to clarify the differences, the limitations and the advantages of each instrument.

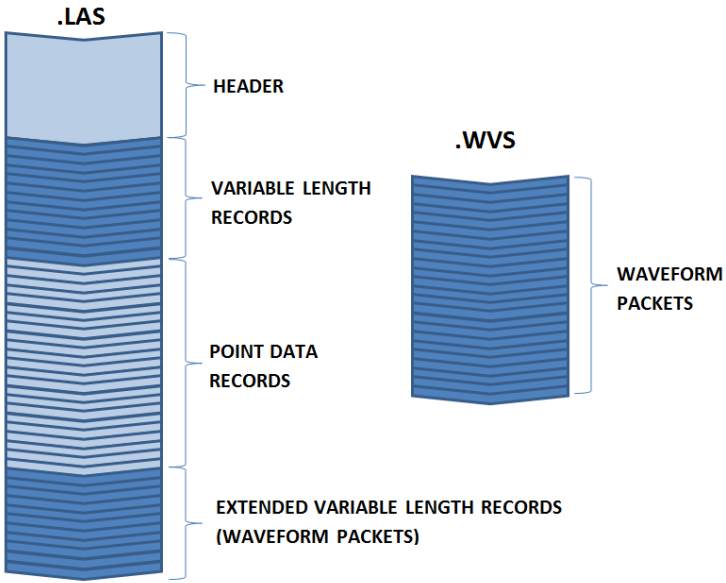


Figure 2-3: How the FW LiDAR data are stored into a binary file, according to the LAS1.3 file format specification

The Trimble performs at a pulse frequency of 400kHz, while the Leica's maximum pulse frequency is 120kHz. Nevertheless, during experiments there were occasions when the Leica discarded every other waveform due to I/O limitations despite being at or below the maximum pulse frequency [19]. The New Forest dataset has been affected by this and, on average, one third of the saved pulses only contain discrete data. We should therefore be extremely careful when comparing Discrete with FW LiDAR data. While [16] concludes that FW LiDAR data worth the extra processing because they have a better vertical profile, [20] states that extra information (the echo-width) from the FW LiDAR data are relatively unimportant. But the New Forest datasets were used for the comparison at [20] and there is no mention about the significantly less waveforms recorded in comparison to the discrete data. It is therefore suspected that their results has been affected by the missing waveforms.

Another problem with the Leica sysyem is the small dynamic range of intensities due to the number of bits used for recording them; the Leica system uses 8-bit integers (0-255 range) while the Trimble uses 16-bit integers (0-16385 range). For increased dynamic range and finer intensities without doubling storage costs, Leica introduced an Automatic Gain Controller (AGC). The AGC is an 8-bit number that defines how the recorded intensity range is shifted across a wider range of intensities. The AGC value is adjusted according to the reflected laser intensity of the previous 64 pulses and it therefore varies across a flightline. Consequently, the raw intensities are incomparable

to each other and, since the relation between AGC and the intensities is not linear, the range normalisation is complicated [21] [22]. In this thesis, the intensities of the Leica system are used as boolean values (whether something existed or not, using a user-defined threshold) to quickly overcome that issue and focus on the major research objectives. Regarding the Trimble instrument, there is no AGC value because the intensities are saved into a 16bit integer and as long as the flight height is constant no normalisation is required. In a few words, the raw intensities recorded using the Leica system are not normalised and therefore not comparable to each other, while the intensities of the Trimble instrument are more meaningful.

The footprint of the laser on the ground depends on the scanning pattern of the instruments and the field of view. The sinusoidal scanning pattern of the Leica system results in a higher density of returns at the edges of the flightline. The footprint of the Trimble instrument is more equally spaced because they are scanned using a rotating polygon. The uneven density pattern of the Leica system is resolved by normalisation during the voxelisation process, but the Trimble's equally spaced pulse pattern is more prone to aliasing when voxelised. Regarding the field of view, the Leica is wider but both systems avoid large angles because otherwise data look deformed at edges of the flightlines.

Last but not least, the Trimble instrument is a native full-waveform sensor; the discrete LiDAR are produced by extracting peak points in post-processing. Therefore one of the purported advantages of a FW system, the concept of extracting a denser point clouds using Gaussian decomposition [13], does not apply in the Trimble's case. This was proven by extracting peak points from Trimble FW LiDAR data using the pulseextract from LAStools [23]; the number of points extracted was exactly the same as the number of points saved into the associated discrete LiDAR files. Therefore discrete data from the Trimble instrument are the same as those generated by echo decomposition and peak points extraction from the FW samples.

To sum up, the Trimble AX60 instrument is a newer sensor and therefore has less problems or design compromises in comparison to the Leica ALS50-II instrument. Table 2.1 summarises the differences between the two sensors.

2.4 Hyperspectral Imagery

Hyperspectral imagery has a positive impact in remote sensing because it contains information beyond human visibility. The human eye receives light from the visual spectrum into three bands (red, green and blue). The hyperspectral sensors captures a larger spectrum and divides its light components into hundreds of bands, recording

Table 2.1: Specifications of the LiDAR instruments used

Instrument Name:	Leica ALS550-II	Trimble Ax60
Scanned Area	New Forest, UK	RedGum, Australia
Year of Introduction:	Discrete LiDAR 2009 & FW LiDAR 2010	2013
Max Scan Frequency (kHz):	120	400
Recorded Intensity (bits):	8	16
AGC:	Yes	No
Scanning Pattern:	Sinusoidal	The footprints are more equally spaced on the ground
Max field of view (degrees):	75	60

this way more information than a human eye can receive [12].

Nevertheless, there are other compromises - for example, the time taken to integrate incoming light as the aircraft carrying the sensors moves. This means the raw airborne images appear deformed because the pixel length varies across the flightline. NERC-ARF geo-corrects the data using the Airborne Processing Library (APL) [24]. The processing levels are numbered. At ‘level 3’ (world coordinate system) the pixels are equally spaced and sized, which requires resampling and thus may look slightly blurred. The ‘level 1’ data (what the sensor saw) are non geo-corrected but they are associated with a file that defines the spatial location of each pixel. In this thesis, the ‘level 1’ data are used to preserve the highest possible quality.

In practise, the level 1 data are held in two files, the ‘.bil’ and the ‘.igm’. The ‘.bil’ file contains the hyperspectral cube (Figure 2-4), all the pixel values at different wavelengths, and the .igm file gives the x, y, z coordinates of each pixel.

The number of bands and the spectrum range captured depends on the hyperspectral sensor. The data from New Forest were collected using the following instruments:

- the Eagle, which captures the visible and near infra-red spectrum (400-970nm)
- the Hawk, which covers short wave infra-red wavelengths (970-2450nm)

Both sensors divide their spectral range into 252 bands (programmable) and each band is a 2D vector as shown in Figure 2-4).

The hyperspectral images also come with a number of drawbacks. A few are mentioned here but since hyperspectral imagery is not the main focus of the thesis there are not addressed:

- System faults sometimes occurs and the affected areas are masked out. This results in blank areas.

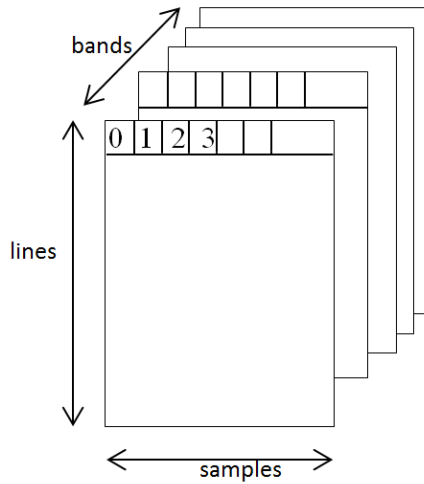


Figure 2-4: This figure shows the order of the hyperspectral pixels saved into the the binary .bil file.

- As a passive sensor, it is dependent on the sun for illumination and thus vulnerable to poor weather conditions
- Due to the high refraction of light at some wavelengths, some bands are highly influenced by humidity (i.e. wavelength 1898.33nm).

To sum up, hyperpsectral images contain information beyond the visible and they are delivered in two files, one contains the hyperspectral cube and the other one the geo-locations of each pixel. In this project, they are used in chapter (Chapter 7), where it is shown that the combination of Remote Sensing data confers better results for generating tree coverage maps.

Chapter 3

Overview of Thesis

Chapter 4

The open source software DASOS and the Voxelisation Approach

Chapter 5

Surface Reconstruction from Voxelised FW LiDAR Data

5.1 Introduction

To briefly sum up the previous sections, FW LiDAR data (Section 2) are laser scanning data particularly useful in Forestry, but the huge amount of information recorded make handling of the data difficult. The open source software DASOS (Section ??) was developed along with this thesis to ease the usage of the data. DASOS voxelises (Section ??) the data before interpretation and this approach is fundamentally different from the related and state-of-art software packages. The output of the voxelisation is a 3D discrete density volume.

In order to visualise a voxel volume, it must be rendered in some form. This chapter explains the process of reconstructing the surface of the scanned area from the 3D voxelised FW LiDAR. At first, volumetric rendering¹ approaches are briefly explained at Section 5.2. Section 5.3 gives a mathematical definition to the voxelised data, while Section 5.4 describes the actual algorithm of extracting a surface. By the end the results are given in Section 5.5.

5.2 Rendering Approaches of Volumetric Data

Even though the concept of visualising 3D discrete density volumes (Volumetric Visualisations) is new in forestry and remote sensing, it has been widely researched in medical imaging and visual effects. There are two approaches to visualising volumetric data.

¹Volumetric rendering refers the process of visualising 3D Volumes.

The first approach is direct rendering, which repeatedly generates 2D images according to the view point (the camera). It is like "taking photos" from a camera and putting them in a sequence to produce an interactive video. An example of direct rendering approach is ray-tracing. Ray-tracing generates images by "taking photos"; rays are cast from the view point, passing through each pixel on a screen and carrying on into the volume. Intensity values are assigned to the pixels according to the nearest intersections [37]. Ray-tracing can be time expensive depending on the complexity of the scene and for that reason some of the literature focuses on parallelising the ray-casting process. By introducing parallelisation, real time rendering of small volumetric data (256^3) was achieved by Pfister et al in 1999 [38]. Also, after the release of the CUDA hardware (which is a parallel computing platform on recent nvidia graphics cards), Crassin et al achieved real-time rendering of billions of voxels in 2009 [39].

The second approach is rasterisation, which is a method that maps primitive polygons (typically triangles) to pixels. It is widely used in computer games, supported directly by common hardware acceleration systems and it is significantly faster than ray-tracing. Furthermore, interactive operations (e.g. measuring the distance between two trees) are trivial calculations on primitives/polygonal meshes and they are easy to implement. In order to use this approach with volumes, they must be first converted to primitives. This is commonly accomplished by surface reconstruction, referring to the extraction of a polygonal mesh, which is a set of primitives like triangles, from the volumetric data. Constructing a surface may take several minutes, but real time visualisations of polygonal meshes are supported by free animation packages (like Blender and Meshlab), in addition to being easy to implement. So, even though it is possible to implement real-time interactive environments using direct rendering of the big voxel data, volumetric visualisation of FW LiDAR data is a new concept in remote sensing and, for simplicity, this thesis uses surface reconstruction.

5.3 Algebraic Definition of the Volume

In computer graphics, objects can be defined using a function rather than being constructed from primitives. Those objects are called either implicit or algebraic. Implicit representation of objects enables a mathematical definition of the 3D discrete density volume generated from the FW LiDAR data (Section ??).

Algebraic objects were firstly introduced in computer graphics by Blinn in 1982 [40] to enable the definition of complex objects without saving a large amount of primitives; in some cases, primitives cannot accurately represent a shape (e.g. a sphere cannot be represented fully by a triangle mesh). Each object is defined by a function $f(X)$ and

the iso-surface value α . The iso-surface value (iso-level) defines the boundaries of the object; for an object $[f(x), a]$ every n-dimensional point X that lies on the surface of the object satisfies the condition $f(X) = \alpha$. To be more accurate, the following rules apply according to Pasko et al [41]:

- $f(X) = \alpha$, when X lies on the surface of the algebraic object
- $f(X) > \alpha$, when X lies inside the algebraic object and
- $f(X) < \alpha$, when X lies outside the algebraic object

Regarding the algebraic representation of the 3D voxelised FW LiDAR data, X is a three dimensional point (x, y, z) representing the longitude, latitude and height respectively and $f(X)$ is a function that takes X as input and returns the accumulated intensity value of the voxel that X lies inside. Also, the iso-surface value α is a user defined parameter. Even though it closely related to the noise threshold used for filtering during voxelisation (Section ??), it is different. The noise threshold filters low intensity samples before the volume is constructed, while the iso-surface value defines the boundaries of the object and it can be modified after the voxelisation because it doesn't affect the intensity values of the 3D voxelised FW LiDAR. Figure 5-5 demonstrates how the iso-level parameter affects the output of the surface reconstruction of the voxelised FW LiDAR data in comparison to the noise filtering.

5.4 Surface Reconstruction with the Marching Cubes Algorithm

Even though numerical implicitisation is beneficial in reducing storage memory, visualising implicit objects is not straight forward, since they contain no discrete values. As described above in rendering volumes, this problem can be addressed either by direct rendering or surface reconstruction (Section 5.2).

The Marching Cubes algorithm is an algorithm that polygonises implicit objects using a look up table. Let's assume that $f(X)$ defines an implicit object. At first the space is divided into cubes. Each cube is defined by eight corner points and each corner point lies either inside or outside the implicit object. By enumerating all the possible cases and linearly interpolating the intersections along the edges, the surface of the implicit object is constructed [42]. The output is a polygonal mesh, a number of adjacent triangles constructed according to the user-defined iso-surface value α of the implicit object.

The normals² are calculated afterwards. According to Lorensen and Cline [42], the normal of each vertex is calculated by measuring the local gradient change. Even though this work well on smooth object (e.g. a sphere defined by its equation), because of the high gradient changes in the voxelised FW LiDAR data this algorithm results into normals pointing into inconsistent directions. This is a problem because when the normals are not consistent, the surface of the object appears rough. For that reason, in DASOS the normal of each vertex is derived by the average normal of its adjacent triangles.

Additionally it is worth highlighting that the sampling of the Marching cubes is independent from the sampling of the 3D density volume. But consistency between the two is required to avoid artefacts. Let's assume the discrete volume has $(n * m * k)$ voxels, then the suggested sampling of Marching Cubes is $((n+1) * (m+1) * (k+1))$, as shown on Figure 5-1; the black grid represents a 2D density grid and the blue grid represents the suggested sampling of the polygonisation. Please note that every point that lies outside the volume is considered to be outside the implicit object. Figure 5-1b shows the effects of oversampling on a low resolution 3D density volume. On the right image the sampling of the volume appears as linear lines and squares on the forested areas because of the Marching Cubes' oversampling. Even though the right polygonal mesh looks blurred, it has been correctly sampled and the blur is because of the low resolution of the volume. Nevertheless there are no geometrical shapes on forested areas and once the resolution is increased then blur will disappear.

5.5 Results

The output of DASOS is a polygonal mesh exported into a .obj file, which is a standard graphics format. The .obj files can be loaded into various animation software tools like Maya and Meshlab (figure 5-2). Figure 5-3 shows polygonal meshes generated using NERC-ARF data from three different areas in the UK. The region of interest is also user defined. The user defines whether an entire flightline or selected area is polygonised (figure 5-4).

Furthermore, there are three main user-defined parameters and figure 5-5 shows how the results are affected once modified:

1. The voxel length controls the resolution of the output; the bigger the voxel length is the lower the resolution and the number of cubes are.

²A normal is a vector that is perpendicular to the surface of a polygonal mesh. In graphics, the normals are important for calculating light illumination and each vertex is associated with one for smooth rendering of surfaces.

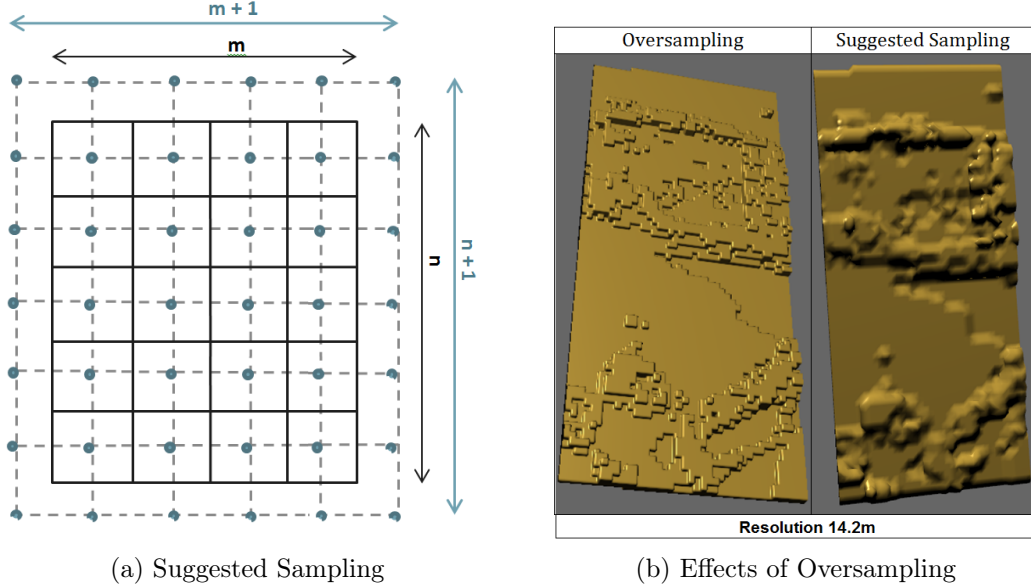


Figure 5-1: The suggested sampling during polygonisation using the Marching Cubes Algorithm

2. The iso-level is the boundary that defines whether a voxel is inside or outside the implicit object. When the iso-level is increased, the number of voxels that are considered inside the implicit object decreases. For that reason, when it is too high most of the voxels are outside the boundary and the object seems to disappear.
3. The noise level is the threshold of the low level filtering applied during voxelisation (Section ??). If the noise level is too low, then the noise covers significant features of the data and when it is too high important information are discarded and the object seems to disappear again.

Aside from computer-based visualisation, it is even possible to 3D print the meshes using something like MakerBot. There are some difficulties as the meshes are not manifold³ (figure 5-6). Simplification of the mesh would have eased the processing of the .obj file in MakerBot.

³A non-manifold polygonal object may have triangle below the outside surface of the object

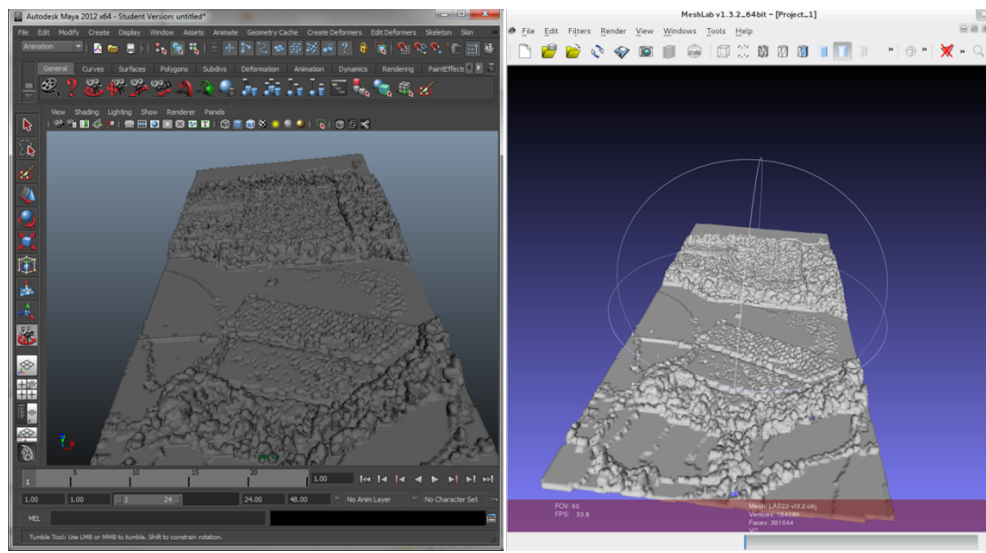


Figure 5-2: Visualising the output of DASOS into animation software packages (Maya and Meshlab)

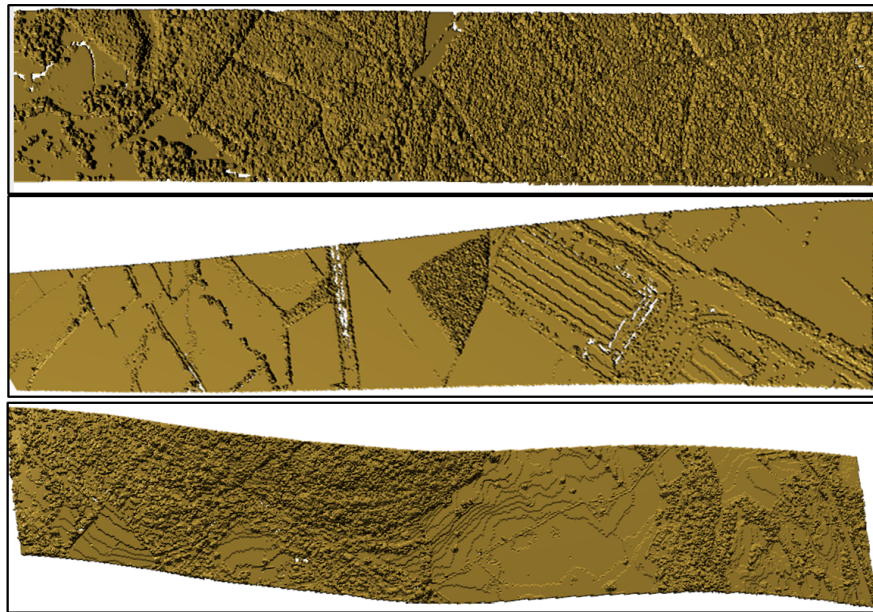


Figure 5-3: Polygonising NERC-ARF FW LiDAR data captured at different areas (New Forest, Milton Keynes and Eaves Wood)

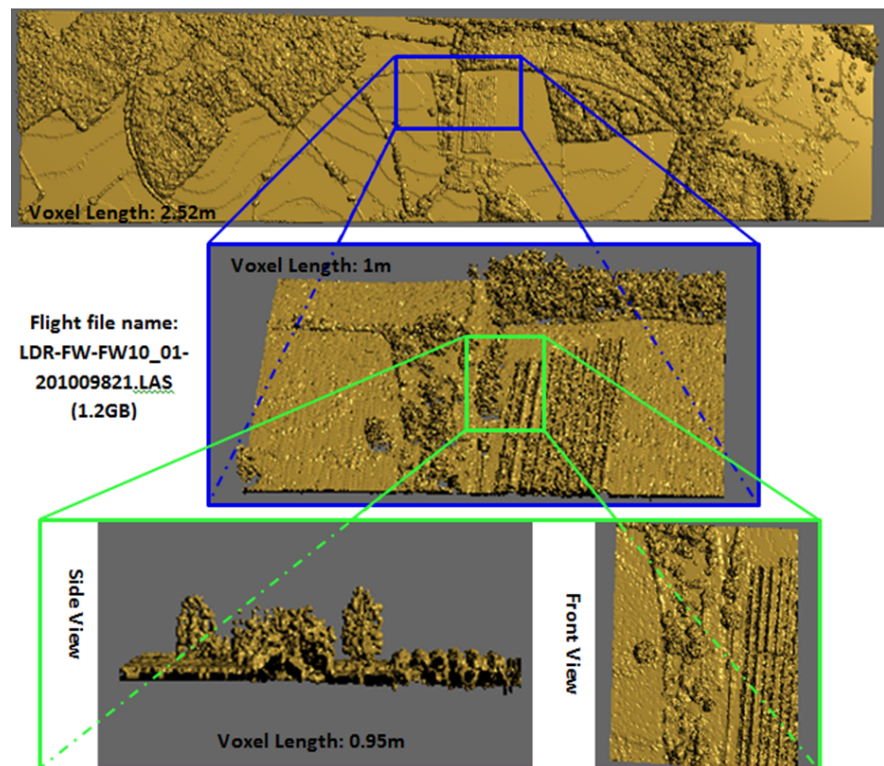


Figure 5-4: Selecting Region of Interest

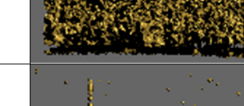
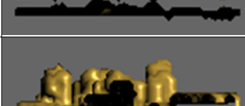
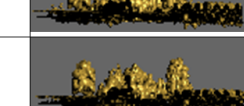
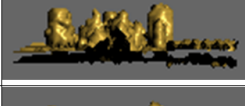
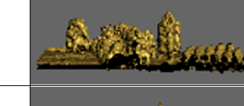
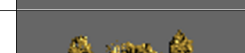
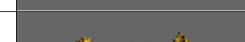
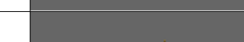
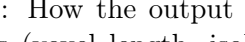
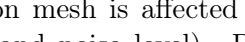
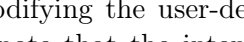
Voxel Length	Visualisation with different voxel lengths	Iso-level *	Visualisations with various isolevels	Noise Level	Visualisations with various noise levels
16.67 m		60		0	
10.0m		45		5	
7.14m		30		10	
5.7m		15		15	
4.44m		0		17	
3.33m		-15		20	
2.5m		-30		25	
2.0m		-45		30	
1.43m		-60		40	
1.2m		-75		60	
1.0m		-85		75	
0.8m		-95		100	
0.67m		-100		135	

Figure 5-5: How the output polygon mesh is affected by modifying the user-defined parameters (voxel length, isolevel⁴ and noise level). Please note that the intensities were scaled to be within the range [-100,100] and that the currently released version of DASOS does not scale the intensities.

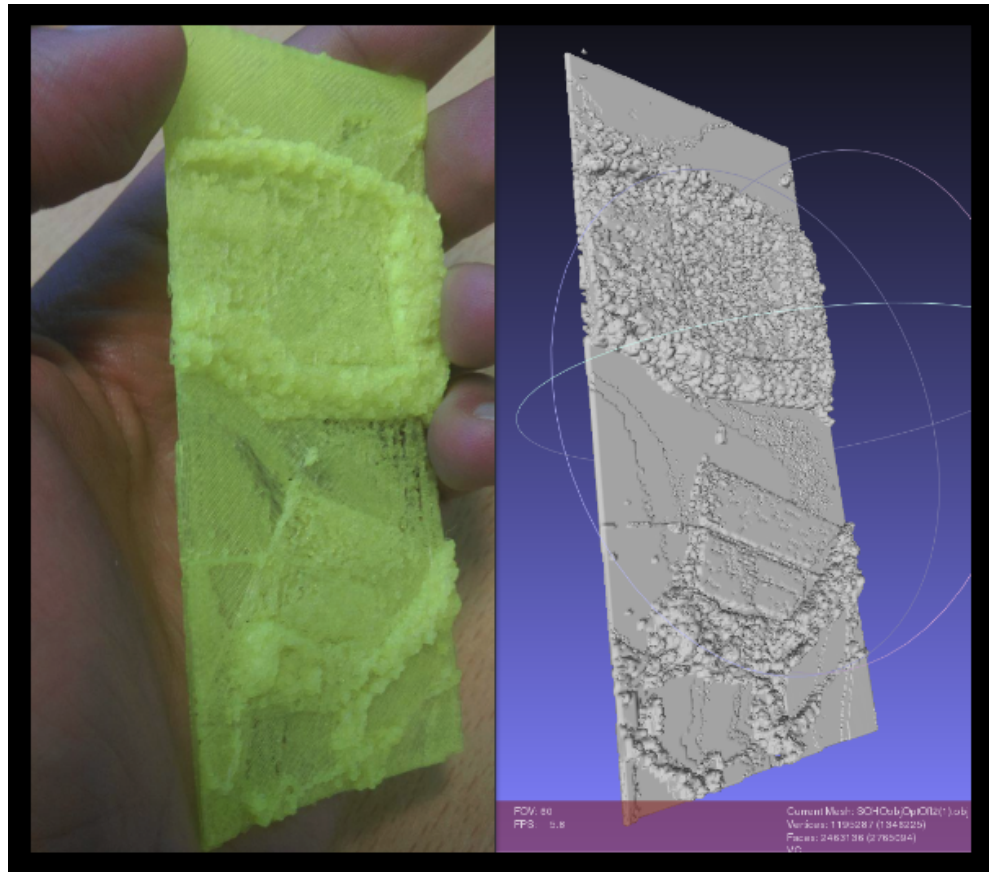


Figure 5-6: 3D printing of New Forest FW LiDAR data

Chapter 6

Optimisation Attempts for the Surface Reconstruction

6.1 Problem and Challenges

While Section 5 explains a simple approach of extracting a polygonal surface from the voxelised FW LiDAR data, this section is mainly focused on objective No. 5 from table (??); it tests how well different data structures performs on the surface reconstruction and it attempts to improve the interpretation of volumetric data by introducing new data structures. The main challenges raised for this task are because the input data are real laser scanning data that contain noise. Some of the challenges that this chapter attempts to tackle are listed below:

1. The LiDAR sensors are vulnerable to clouds and seagulls being misinterpreted and recorded as hit points. Those outliers are much higher than tree canopies but they are within the boundaries of the scanned area. As a result, on average 96% of the voxels are empty.
2. Marching Cube is a scan line algorithm, which implies looping through every single voxel, including the empty ones. This is very time consuming and therefore, algorithms that quickly identify and ignore empty areas are essential.
3. While loading an entire volume, the huge amount of empty voxels may lead into exceed usage of memory. It is therefore preferable to store the voxels into a hierarchical structure that avoids storing the empty ones.
4. When extracting a surface from real data, it is very likely to generate non-manifold objects. Non-manifold objects are not homeomorphic to Euclidean 1-space be-

cause they have crossing points. This also occurs at the polygonal meshes generated by DASOS as explained at Chapter 5.

6.2 Related work

6.2.1 Full-Waveform LiDAR Visualisation

Summarising previous aforemoneted related work (Section ??), traditional ways of interpreting the full-waveform LiDAR data suggest echo decomposition for detecting peak points and interpreting the point clouds extracted [28]. Both SPDlib [32] and FullAnalyse [31] visualises either the peak extracted points or the raw waveform samples. On the one hand, SPDlib visualises the samples as points with intensity above a given threshold, while FullAnalyse generates a sphere with radius directly correlated to that intensity of each wave sample. Similarly, Pulsewaves visualises a number of waveforms with different transparency according to their intensity [25]. On the one hand, visualising all the wave samples makes understanding of data difficult due to the high noise. On the other hand, peak point extraction identifies significant features but the FW LiDAR data also contain information about echoes width. These information can be accumulated from multiple shots into a voxel array, building up a 3D discrete density volume [34].

Voxelisation of FW LiDAR data was introduced by [26] who used it to visualise small scanned areas (15mx15m). The waveforms samples were inserted into a 3D Voxelised space and the voxels were visualised using different transparencies according to their intensity. Similarly, as explained at Section ??, we adopt voxelisation for surface reconstruction and applied it on larger areas. Once the 3D density volume is generated, numerical implicitisation is used to represent the scanned area. Nevertheless, visualising numerical/implicit objects is not straight forward, since they contain no discrete values (Section 5.3). This problem can either be address by ray-tracing [37] or polygonisation [42]. At this thesis, the polygonisation direction is taken, as explained in Section 5.4. This chapter introduces new ways of interpreting real voxelised data and tests how well six data structures performs on surface reconstruction.

6.2.2 Optimising Volumetric Iso-surface Extraction

Even though volumetric visualisation has only been recently used for FW LiDAR systems, there are many applications in medical visualisation [43] [44] and visual effects [39] [45]. Research work exists on optimising both ray-tracing and surface reconstruction and it can be categorised into three groups: surface-tracking, parallelisation

and data structures. Those approaches are discussed below along with their benefits and limitation in respect to voxelised FW LiDAR data.

Surface-tracking was applied at [46] [47]. Starting from a seed point, the surface is expanded according to the local curvature of the implicit object. This method is considered to be faster and more efficient in comparison to the Marching Cubes algorithm since huge empty spaces are ignored. It further opens up possibilities for finer surface reconstruction at areas with high gradient changes. Nevertheless, surface-tracking algorithms cannot be applied with real laser scanning data because these data are neither manifold or closed. For example in a forest scene, a tree may be detached from the ground due to missing information about its trunk. Therefore by tracking the surface, the algorithm may converge at a single tree instead of the entire forest.

Hansen and Hinken proposed parallelising the polygonisation process of BlobTree trees on Single Instruction, Multiple Data (SIMD) machines [48]. On SIMD machines greater speed up is achieved at longer instruction. BlobTree trees represent implicit objects as a combination of primitives and operations [49]. While the depth of the tree increases, the length of the instruction increases as well. Nevertheless the function at the implicit representation of the FW LiDAR data at [34] is executed at constant time, making it harder to achieve speed up using SIMD machines. Further, according to the C++ Coding Standards when optimisation is required is better to seek an algorithmic approach first because it is simpler to maintain and less likely to contain bugs [50].

Hierarchical data structures, like octrees, improves the performance of the isosurface extraction because of the huge amount of empty voxels that can be ignored during polygonisation [51]. The literature in the data structures direction aims to either simplify/improve the output mesh, optimise traversal time of hierarchical data structures or eliminate hierarchy. For example, the extraction of locally finer details either with dual grids [52] or edge-trees [53] reduces the amount of vertices produced. In addition, a net of linked surface nodes improved anti-aliasing and reduces artifacts of 3D Magnetic Resonance Imaging (MRI) [54]. Regarding efficiency of accessing data, fractional cascading slightly improved time complexity of range queries [55]. Sparse Voxel Octrees improved efficiency by having a pointer pointing to children and packing children coherently in memory [45]. Hadwiger et al uses a 3D virtual memory to keep voxels coherent on GPU and avoid traversal [44]. Nevertheless, due to the adjacency of neighbouring voxels, data are saved for empty voxels yielding into much wasted memory. OpenVDB library arranges blocks of grids into a B+ hierarchical data structure for increased cache coherency and lower tree depth [56]. The bricks structured used at GigaVoxels is similar in terms of blocks, named bricks, and it's been used for efficient GPU ray-casting [39]. For eliminating tree traversal time, Warren and Salmon introduced hash octrees for N-

bosy simulation of particles [57]. Similarly, voxel hashing was proposed for overheading the traversal time of hierarchical structures and real time surface reconstruction was achived using depth cameras online [58]. Most of those data structure optimisations are based on GPU processing, but they are still very relevant.

6.3 Overview

This thesis compares six approaches for handling and polygonising voxelised full-waveform LiDAR data. The first three approaches use data structures from the literature and the scan line Marching Cubes algorithm. An explanation of their functionalities is given at Table 6.1. The last three approaches are more complicated because they take into consideration the chunks of empty voxels and ignore them during surface reconstruction. A brief summary of them is given in Table 6.2 and they are fully explained in Section 6.4. Please note that the "1D Array" is the original implementation, while each one of the other five approaches tackles at least one of the aforementioned challenges (Section 6.1).

1D Array	Voxel Hashing	Octree
Influenced by [44], all the data are saved into an 1D array to guarantee coherent memory, even though much memory is wasted in regards of empty voxels.	The intensities of the voxels are saved into a simple hash table with key value relevant to their position into the volume. Similary to [58], this approach overheads traversing time of hierarchical structures and on top of that it reduces memory allocation because empty voxels are not stored.	This is a traditional hierarchical octree with traversal time to be essential. Please note that this is a scan line test and therefore it does not take into consideration empty chunks of memory.

Table 6.1: Brief Description of the Three Scan-Line Tests

Integral Volumes	Octree Max and Min	Integral Tree
<p>This data structure is an extension of Integral Images to 3D. It was firstly presented at the CGVC conference and it is a part of this thesis. Using Integral Volumes, the sum of any cuboid area is calculated in constant time. By repeatedly dividing the space into cuboids, big empty spaces are quickly identified and ignored during the surface reconstruction.</p> <p>(Section 6.5)</p>	<p>In this approach, the values are saved into an octree, but the surface reconstruction is build along the tree. This is slightly different than a traditional octree, because at each branch node its max and min values are saved. This way, areas that are completely full or empty are identified during traversal before reaching the leaves of the trees.</p> <p>(Section 6.6)</p>	<p>It is a combination of Octree and Integral where the sum of a given branch is returned at constant time. That was an attempt to combine the idea of Integral Images and Octrees. Nevertheless, traversal time and backtracking for finding neighbouring voxels still exists.</p> <p>(Section 6.7)</p>

Table 6.2: Description of the Three Optimisation Attempts

6.4 The Optimisation Methods

6.5 Integral Volumes

The Integral Volumes optimisation is based on the idea of Integral Images, which is an image representation where each pixel value is replaced by the sum of all the pixels that belong to the rectangle defined by the lower left corner of the image and the pixel of interest. An integral image is constructed in linear time and the sum of every rectangular area is calculated in constant time, as shown in figure 6-1 [59]

In this paper, we extend Integral Images to Integral Volumes and use them to quickly identify and ignore big chunks of empty voxels during polygonisation. The following section explains the mathematics behind Integral Volumes, while sections 6.5.2 and 6.5.3 give an in depth description about the algorithms invented.

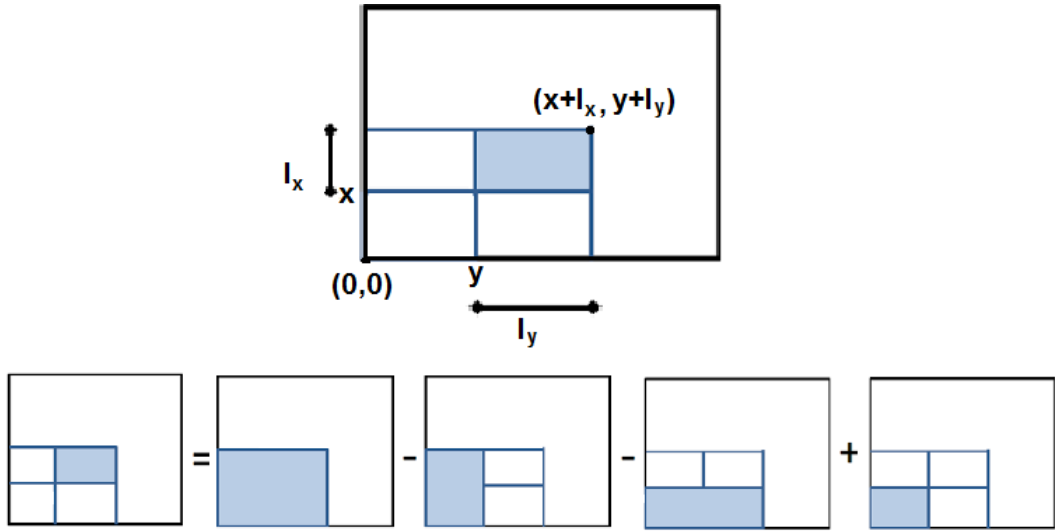


Figure 6-1: Once the Integral Image is constructed, the sum of any rectangular area is calculated in constant time.

6.5.1 Extending Integral Images to Integral Volumes

As shown in Figure 6-1, the area of interest is defined by the pixels (x, y) and $(x+l_x, y+l_y)$ and the sum S is given by:

$$S = T(x + l_x, y + l_y) - T(x + l_x, y - 1) - T(x - 1, y + l_y) + T(x - 1, y - 1) \quad (6.1)$$

where S is the sum of rectangular area of interest, $T(x, y)$ is the value of the integral image at (x, y) and l_x, l_y define the length of the rectangle in the x and y axis respectively.

Extending integral images to 3D, the value of the voxel (x, y, z) in a 3D integral volume becomes equal to the sum of all the values that belong to the box defined by the (x, y, z) and $(0, 0, 0)$ included. Therefore the sum (S) of the box defined by (x, y, z) and $(x + l_x, y + l_y, z + l_z)$ included is given by:

$$\begin{aligned} S = & T(x - l_x, y + l_y, z + l_z) - T(x - 1, y + l_y, z + l_z) - \\ & T(x + l_x, y - 1, z + l_z) - T(x + l_x, y + l_y, z - 1) + \\ & T(x - 1, y - 1, z + l_z) + T(x - 1, y + l_y, z - 1) + \\ & T(x + l_x, y - 1, z - 1) - T(x - 1, y - 1, z - 1) \end{aligned} \quad (6.2)$$

where $T(x, y, z)$ is the value of the voxel (x, y, z) in the 3D integral volume. S is the sum of voxels inside the box, $T(x, y, z)$ is the value of the voxel (x, y, z) in the

3D integral volume. and l_x, l_y, l_z define the length of the box in the x , y and z axis respectively.

6.5.2 Optimisation Algorithm

As mentioned before, using Integral volumes empty areas are quickly identified and ignored during polygonisation. An iterative algorithm is introduced here. This algorithm continuously splits the volume and checks whether the sub-volumes and its neighbouring voxels are empty using the Integral Volumes. Please note that all the values below the threshold boundary of the object must be zero and all the non-empty voxels must contain a positive value.

Algorithm 1 Integral Volumes Optimisation Algorithm

```

1: Push the entire Volume as a cuboid inside a Stack
2: while stack is not empty do
3:   Cuboid-A  $\leftarrow$  next cuboid from the Stack
4:   if Cuboid-A and neighbours are empty then
5:     discard Cuboid-A
6:   else if Cuboid-A consists of only one cube then
7:     polygonise Cuboid-A
8:   else
9:     divide Cuboid-A
10:    push the two new Cuboids into stack

```

Here it is worth highlighting that, on line 3 of the algorithm it is checked if the neighbouring cubes of a cuboid are empty, because the voxels of the 3D density volume and the cubes in marching cubes algorithm are aligned with an offset (Figure 5-1a). If volumes with non-empty neighbouring voxels are ignored, then holes appear on the output polygon mesh.

6.5.3 Coding Details for Faster Implementation

Implementation details contributes to the efficiency and speed up of the algorithm. Significant improvements are achieved by reducing recursions, big memory allocations and if statements, since memory jumps are time expensive. As shown in algorithm 1, a while loop is used to avoid recursion. In this section it's given an explanation on how the stack controls memory consumption and how bitwise operations reduces if-statement usage.

Regarding memory consumption, a stack was chosen over a queue, to decrease the amount of cubes saved into the data structure simultaneously. A queue is a first in first out data structure, while a stack accesses data in a last in first out order. In every

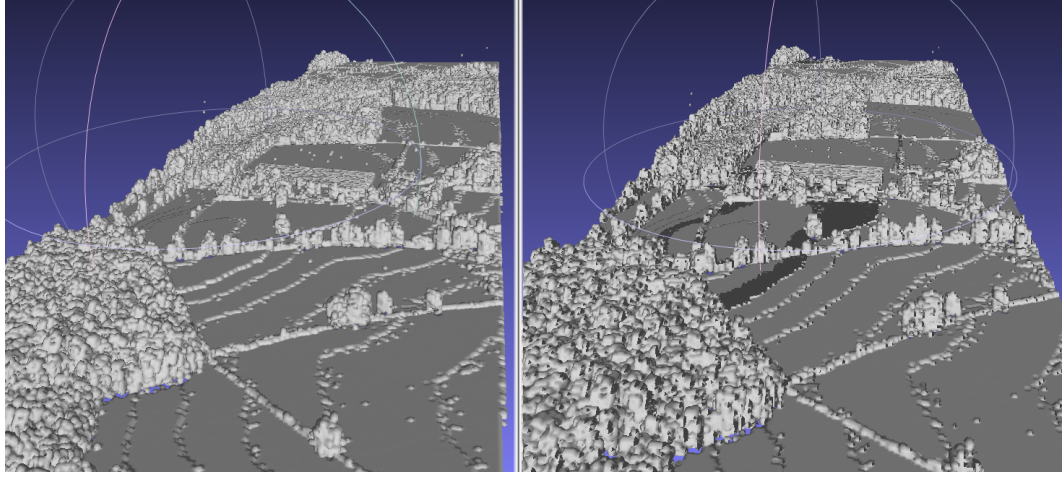


Figure 6-2: Comparison between including and ignoring neighbouring voxels; holes appears when ignored.

iteration, it is ideal to interpret the smallest saved cube, such that the possibility of being polygonised is higher and the possibility of storing another cube is less. A queue guarantees cubes with approximately the same size, since the big cubes will be added first and sequentially being divided first. In contrast, a stack guarantees the smallest possible number of cubes saved. The larger cubes are stored in the bottom of the stack while the smaller ones are interpreted first because they are always the last one divided and inserted into the stack. For that reason, a stack guarantees the lowest memory usage.

Furthermore, in algorithm 1 an issue exists: how to quickly identify the side to be divided next? Ideally, the usage of if-statements should be low because they contains many time expensive memory jumps. For that reason, bitwise operations were embedded into the program to reduce their usage. A cube is defined with its position, its size, the next side to be divided s and its divisible sides D . The parameter s takes the values 1, 2, 3 for the x , y , z sides respectively. The parameter D is an integer consisting of the sum of three numbers (1 or 0) + (2 or 0) + (4 or 0) indicating whether the sides x , y , z are divisible or not (table 6.3). The parameter D takes the value between [0, 7] and covering all the possible cases of divisible sides as shown in tables 6.4 and 6.5. For example if x and z are the divisible sides, then $D = 1 + 0 + 4 = 5$. By the end, the bitwise operations and the faster implementations of the Integral Volumes optimisations is shown at algorithm 2.

	Decimal Numbers		Binary Numbers	
Side	Divisible	Not Divisible	Divisible	Not Divisible
X	1	0	0001	0000
Y	2	0	0010	0000
Z	4	0	0100	0000

Table 6.3: Values of divisible sides

X	1	-	1	-	1	-	1	-
Y	2	2	-	-	2	2	-	-
Z	4	4	4	4	-	-	-	-
D	7	6	5	4	3	2	1	0

Table 6.4: How to calculate the value of D, which represents the divisible sides of a cuboid

X	0001	-	0001	-	0001	-	0001	-
Y	0010	0010	-	-	0010	0010	-	-
Z	0100	0100	0100	0100	-	-	-	-
D	0111	0110	0101	0100	0011	0010	0001	0000

Table 6.5: How to calculate the value of divisible sides (D) in binary representation

Algorithm 2 Integral Volumes Optimisation Algorithm

```

1: Push the entire Volume as a cuboid inside a Stack
2: while stack is not empty do
3:   Cuboid-A  $\leftarrow$  next cuboid from the Stack
4:   if Cuboid-A and neighbours are empty then
5:     discard Cuboid-A
6:   else if D is equal to 0 then
7:     polygonise Cuboid-A
8:   else if (D bitwise add  $2^s$ ) shift right ( $s - 1$ ) then
9:     divide side s of Cuboid-A
10:    if the new length of side s is equal to 1 then
11:       $D \leftarrow D$  bitwise add ( $7 - 2^s$ )
12:       $s \leftarrow (s + 1) \bmod 3$ 
13:      push both new Cuboids into stack
14:    else
15:       $s \leftarrow (s + 1) \bmod 3$ 
16:      push Cuboid-A back into the stack

```

6.6 Octree Max and Min ****Everything from here is new :)**

Integral Volumes quickly identify and ignore empty spaces during polygonisation (tackles the 1st, 2nd and 4th problem of the original algorithm – Section 6.1), but it allocates memory for the entire volume (the 3rd problem). For that reason, the ‘Octree Max and Min’ data structure has been implemented.

The ‘Octree Max and Min’ data structure avoids storing empty voxels and it also identifies empty areas during polygonisation. The polygonisation is built on the traversal of the octree, as explained in Algorithm 3. Similarly to Integral Volumes, a stuck is used to avoid recursion and reduce memory jumps. While using the Integral volumes, it is checked whether the neighbours of a cuboid is empty or not to avoid generating holes on the polygonal mesh. This is also essential when a branch to be discard at ‘Octree Max and Min’ data structure. But because the every branch of an octree is cubic and power of two, it is not trivial to check whether the neighbours of a branch are empty or not. For that reason, we loop through its edges and polygonise them according to look up table of the the Marching Cubes algorithm.

Algorithm 3 Embedding the Marching Cubes Algorithm into an octree structure

```
1: Push the Root as a Node into a Stack
2: while stack is not empty do
3:   Node-N  $\leftarrow$  next Node from the Stack
4:   if Node-N is a Leaf then
5:     polygonise Leaf
6:   else if Node-N has no children OR max value of Node-N < isolevel
      OR min value of Node-N > isolevel then
7:     POLYGONISE_EDGES_OF_CUBIC_WITH_ROOT_NODE-N()
8:   else
9:     push the children of Node-N into the Stack
```

Embedding the polygonisation of volumetric data into an octree has been done before [51]. Nevertheless, the ‘Octree Max and Mean’ data structure differs in two ways:

- The max and min values of each branch are stored into the corresponding node to speed up polygonisation. This enables checking whether the leaves of a branch lie either only inside or only outside the implicit object¹. If they do, then no iso-surface is crossing that branch and it can be discarded (after polygonising its edges).
- A new algorithm is proposed and implemented for finding neighbouring voxels.

¹Explanation about implicit/algebraic objects is given at Section 5.3

This algorithm reduces comparisons and jumps in memory. An in-depth explanation of this algorithm is given at Section 6.6.1.

6.6.1 Finding Neighbours

Every time a voxel/leaf is polygonised, seven of its neighbours are checked to decide whether a surface is passing through that area or not. At hierarchical data structures, the nearest common ancestor is tracked upwards and the branch, with root the common ancestor, is traversed to reach the neighbour. The article [60] uses recursion that terminates once a common ancestor between a leaf and its neighbour is identified. According to Scharack [61], finding neighbours in linear octree² is done in constant time. Nevertheless, linear Octrees are full octrees. Therefore, if used in our case all the empty voxels would have to be stored as well. Lohner suggested vectorising the space during post-processing for finding the shorter distance between un-constructed points [62]. However, the 3D voxelised FW LiDAR is a regular grid and during polygonisation the shorter distance to travel is one voxel. For that reason simpler approaches with less initialisation time, like [61] could perform equally well. Castro et al. [63] assume that with hierarchical octrees it is not possible to start searching neighbours from leaves and suggest using hashed octrees to do that. In contrast, it is possible to start from the leaves and find the common ancestor using parentship as described at [60].

To avoid recursion and reduce comparison, this thesis introduces a new way of finding the common ancestor using logarithms of 2. The Algorithm 4 explains the proposed method. As shown in Figure 6-3, there are occasions where it is cheaper to start searching a neighbour from the root instead of the leaf. For example Node-*F* is the (+1) neighbour of Node-*E*. If we start looking for it from the leaves then we need to travel through 6 nodes, but if we start from the root we only need to travel 5 nodes. Logarithms helps us decide which route to take, while reducing comparisons (i.e. no need to check whether branches has common faces while travelling upwards [60]).

²Linear octrees are octrees stored into a 1D-array instead of a hierarchical structure.

Algorithm 4 Finding the number of steps required to go upward in order to find the common ancestor of a Leaf(x) of interest and its (+1) neighbour

```

1:  $c \leftarrow \text{ceil}(\log_2 x)$ 
2:  $c_1 \leftarrow \text{ceil}(\log_2(x + 1))$ 
3: while  $c = c_1$  do
4:    $x = x - 2^{(c-1)}$ 
5:    $c \leftarrow \text{ceil}(\log_2 x)$ 
6:    $c_1 \leftarrow \text{ceil}(\log_2(x + 1))$ 
7: if  $D_{\max}/2 < c_1$  then
8:   Start from Root to find Neighbour Branch +1
9: else
10:  Backtrack  $c_1$  parents to find the common ancestor
11:  Find neighbour

```

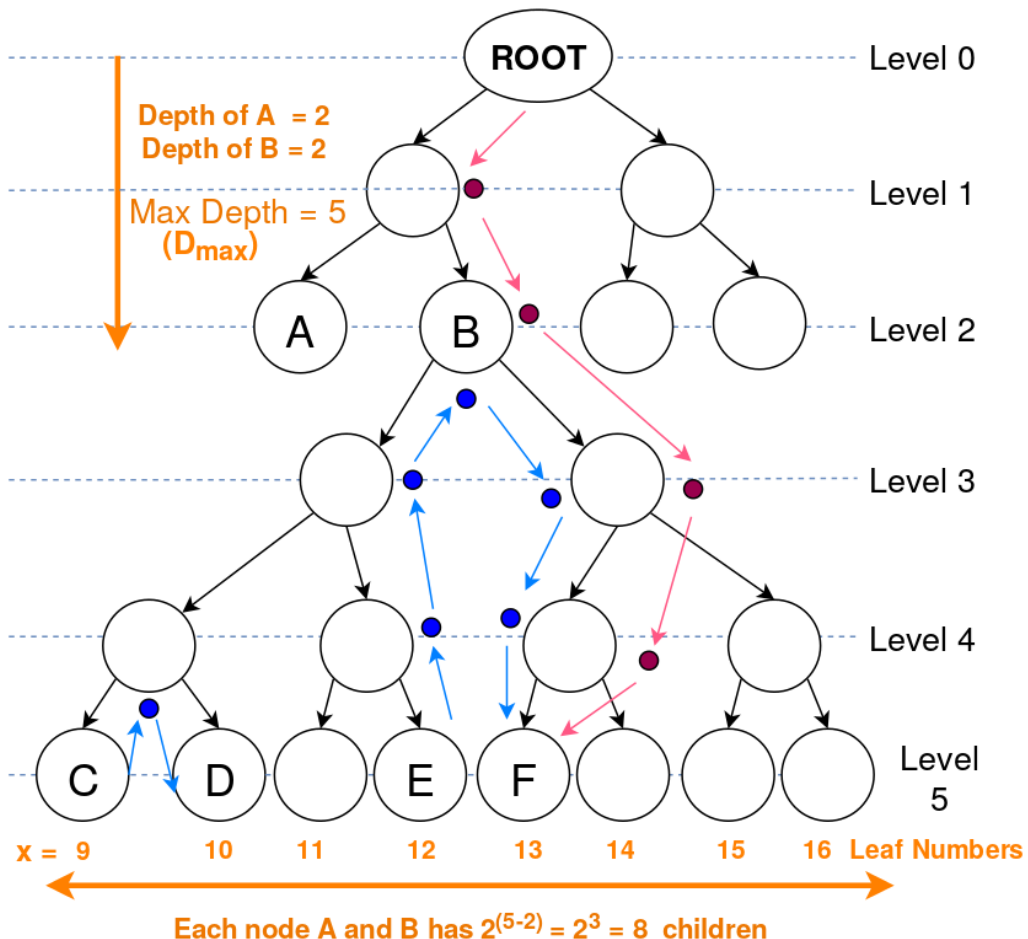


Figure 6-3: This diagram depicts the parameters used for finding neighbouring voxels.

6.7 Integral Tree

6.7.1 Main Idea

The Integral Tree is a new term that describes the attempt to preserve some properties of the Integral Images while using a non-full tree structure. Every Integral Tree consists of two elements: an integral 1D-array and a tree. All the values of every non-empty and non-connecting node are saved into an 1D-array, in a way such that the Integral Tree's condition is fulfil: all the values of every branch B are adjacent inside the 1D-array. Afterwards the array is converted to integral; the sum of every n continuous values is calculated in constant time. Additionally, the root node of each branch B contains two parameters $(*p, k)$. The number k is the number of nodes with values the branch B has (e.g. for an octree, it is all its leaf nodes) and the pointer $*p$ points to the first one in the 1D-array (Figure 6-4).

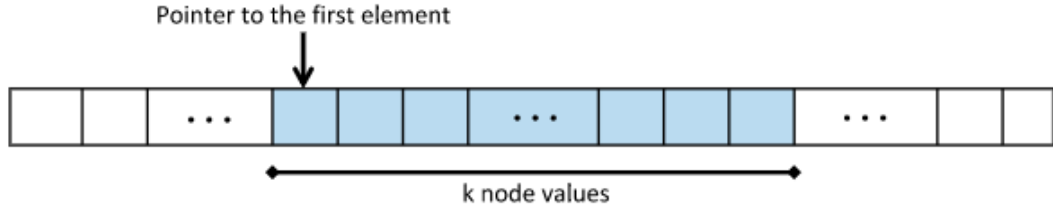


Figure 6-4: Ordering of tree elements

The aforementioned rules can be applied to any tree structures including binary trees, quadtrees and octrees. To better perceive how this data structure works, let's assume that there is a number of 2D spatially distributed values. Figure 6-5 depicts how they can be saved into an Integral Quad Tree in order to fulfil the Integral Tree's condition of adjacency. Also, Section 6.7.2 gives an example of an Integral Binary Tree.

6.7.2 Integral Binary Tree Example

An example of applying the idea of Integral Tree into a binary tree is given for clarity (Figure 6-6). Firstly, the values of the binary tree are sorted into the 1D-array A as $\{15, 12, 10, 13, 14, 17, 16, 18, 19\}$ in order to fulfil the Integral Tree's condition of adjacency. Secondly, the array A is modified as $\{15, 27, 37, 50, 64, 81, 97, 115, 134\}$ in order to become integral using the following equation:

$$A[i] = A[i] + A[i - 1] \quad (6.3)$$

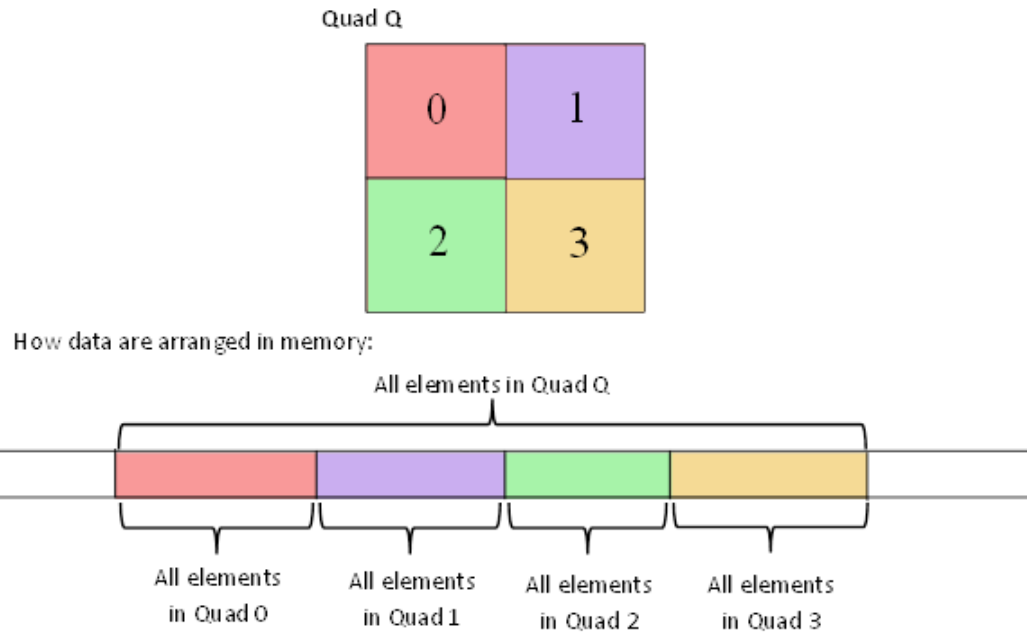


Figure 6-5: Illustration of how to save the values of an Integral Quad Tree into the 1D-array, in order to preserve the condition of Integral Trees

$*p$	0	1	2	3	4	5	6	7	8
1-D Array (1 st step)	15	12	10	13	14	17	16	18	19
1-D Array (2 nd step)	15	27	37	50	64	81	97	115	134

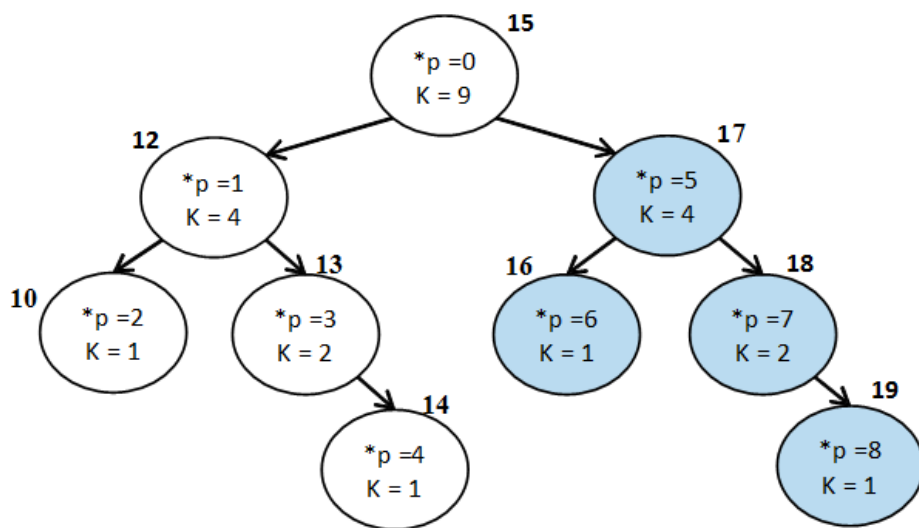


Figure 6-6: Example of Integral Binary Tree

Then, the sum S of each branch with root $*p$ and k -nodes is calculated at constant time as follow:

$$S = A[*p + k - 1] - A[*p - 1] \quad (6.4)$$

For instance the sum of the blue branch on Figure 6-6 is $A[5 + 4 - 1] - A[5 - 1] = A[8] - A[4] = 134 - 64 = 70$, which is correct since $17 + 16 + 18 + 19 = 70$.

6.7.3 Integral Octree for Surface Reconstruction

The same algorithms as 'Octree Max and Min' are used. The only difference is at the comparison of Line 6 at Algorithm 3.

at octree the values saved into the 1-D array are all the leaves of the trees.

The leaves of the octree are saved into the 1D-array.

6.8 Results and Discussion

The following tests first test how well each data structure performs in terms of execution time and memory usage. Different algorithms could either be beneficial in speeding up the process or decrease memory usage.

Time program required to be executed Table single flightline different resolutions

Same resolution, constant noise level, different Flightlines

LDR-FW-FW10_01-201009821.LA

On the one hand, it preserves the lower memory consumption of an octree, but despite Integral Volumes, when using an octree the space should be cubic and finding neighbouring voxels is more complicated and time consuming.

More complicated to pre-save values for faster interpolation.

The Hashed Octree approach could further be used for speeding up neighbouring search in spatial representation of geometric objects.

By the end, even though this new data structure is extremely beneficial for the aforementioned optimisation algorithm (Section 4.4***) and multi-resolution direct volumetric rendering, there is a big drawback associated with it: adding elements to it implies reconstruction of the entire tree. In volumetric rendering of FW LiDAR data, the possibility of adding new elements in the volume is not big and the data of each scan are constant, so this is not a considerable problem for this project. Nevertheless, in the case of cloud simulation in animated movie, this structure would have not been appropriate

due to the time required to reconstruct the tree every time an element is added or modified.

		1D-Array						Voxels Hashing						Octree					
Resolution		Time (s)			Memory			Time (s)			Memory			Time (s)			Memory		
Length (m)	No. of Voxels	Con	Pol	Total	MByte	Con	Pol	Total	MByte	Con	Pol	Total	MByte	Con	Pol	Total	MByte		
20	29x115x23	12.04	0.16	12.21	10.17	12.84	0.19	13.02	9.78	14.58	0.18	14.76	11.07						
15	39x157x30	12.06	0.32	12.38	12.50	12.96	0.37	13.33	11.44	14.91	0.35	15.26	12.00						
10	58x235x45	12.07	0.80	12.87	20.09	12.95	0.96	13.92	16.19	14.92	0.91	15.82	16.69						
5	116x476x89	12.08	4.85	16.92	88.35	13.01	6.95	19.96	47.66	15.26	5.55	20.81	50.50						
4	145x597x111	12.24	9.21	21.45	158.94	13.08	12.83	25.91	76.7	15.58	10.61	26.19	80.31						
3	194x800x148	12.19	21.90	34.09	362.23	13.23	29.94	43.16	153.27	15.67	24.14	39.81	8.27						
2	290x1199x222	12.45	67.65	80.10	1153.13	13.69	95.85	109.54	389.34	16.16	75.29	91.45	417.98						
1.5	387x1602x295	12.83	151.48	164.31	2666.67	13.96	216.35	230.31	788.00	16.26	166.23	182.49	839.35						
1	80x2405x443	14.62	443.5	458.1	8556.78	15.43	672.07	687.50	1912.57	16.91	491.88	508.79	2056.805						
		Integral Volumes						Octree Max/Min						Integral Tree					
Resolution		Time (s)			Memory			Time (s)			Memory			Time (s)			Memory		
Length (m)	No. of Voxels	Con	Pol	Total	MByte	Con	Pol	Total	MByte	Con	Pol	Total	MByte	Con	Pol	Total	MByte		
20	29x115x23	12.9	0.15	13.05	10.38	14.65	0.21	14.86	18.32	14.67	0.23	14.9	18.27						
15	39x157x30	12.11	0.28	12.39	12.8	15.01	0.34	15.35	19.8	14.76	0.37	15.13	20.16						
10	58x235x45	12.17	0.68	12.85	20.43	15.12	0.89	16.01	25.68	15.32	0.92	16.24	25.93						
5	116x476x89	13.62	3.56	16.02	88.84	15.3	4.99	20.29	67.5	15.98	5.03	21.01	68.94						
4	145x597x111	13.32	6.48	19.81	159.08	15.62	9.45	25.07	110.24	16.45	9.67	26.12	117.25						
3	194x800x148	15.15	14.37	29.52	363.95	15.74	26.16	41.9	218.92	16.51	26.35	42.86	231.67						
2	290x1199x222	23.11	40.8	63.91	1154.02	16.21	63.02	79.23	595.01	17.14	64.08	81.22	720.01						
1.5	387x1602x295	39.64	86.54	126.18	2667.67	16.37	131.21	147.58	898.8	19.22	133.46	152.68	968.43						
1	80x2405x443	111.38	210.94	322.32	8559.66	17.91	348.97	366.88	2087.71	25.83	352.31	378.14	2123.14						

Table 6.6: Results: Execution time and memory consumption, Con=Construction, Pol= Polygonisation, MByte=Max Memory

		1D-Array						Voxels Hashing						Octree					
Resolution		Time (s)			Memory			Time (s)			Memory			Time (s)			Memory		
Length (m)	No. of Voxels	Con	Pol	Total	MByte	Con	Pol	Total	MByte	Con	Pol	Total	MByte	Con	Pol	Total	MByte		
6	96x250x76	6.70	2.10	8.80	51.70	7.05	2.61	9.66	29.94	7.70	2.33	10.02	32.15						
3	191x561x149	6.61	14.82	21.43	275.71	7.21	19.95	27.16	107.61	7.98	15.71	23.70	110.96						
1.5	381x1122x296	7.11	104.51	111.62	1810.67	7.95	154.10	162.05	428.18	8.70	109.54	118.25	451.41						
6	100x760x64	30.34	6.32	36.66	114.00	38.03	8.16	46.19	78.57	40.27	6.85	47.11	79.90						
3	199x1525x124	30.25	48.58	78.83	766.74	33.84	64.90	98.73	424.13	40.27	54.89	95.17	437.93						
1.5	398x3063x248	30.82	310.93	341.75	4776.21	35.03	434.00	469.04	1659.12	40.77	342.88	383.65	1754.78						
6	382x90x108	30.78	3.58	34.36	79.26	33.43	4.47	37.90	45.43	40.76	4.04	44.79	46.00						
3	763x178x213	30.23	23.81	54.05	462.16	33.53	34.82	68.35	179.23	41.38	26.04	67.42	186.75						
1.5	1526x355x424	30.70	195.64	226.34	3261.54	34.99	298.46	333.45	896.38	41.99	197.40	239.40	962.02						
		Integral Volumes						Octree Max/Min						Integral Tree					
Resolution		Time (s)			Memory			Time (s)			Memory			Time (s)			Memory		
Length (m)	No. of Voxels	Con	Pol	Total	MByte	Con	Pol	Total	MByte	Con	Pol	Total	MByte	Con	Pol	Total	MByte		
6	96x250x76	9.20	1.28	10.48	51.19	9.40	1.67	11.07	31.50	7.17	2.07	9.25	30.88						
3	191x561x149	8.89	8.04	16.93	275.76	7.51	9.89	17.40	111.52	7.06	11.33	18.40	105.68						
1.5	381x1122x296	25.76	46.48	72.23	1810.99	7.49	55.73	63.22	443.09	7.34	59.60	66.94	417.36						
6	100x760x64	31.81	4.50	36.31	114.24	35.26	6.09	41.35	82.86	35.23	6.70	41.93	68.93						
3	199x1525x124	34.76	34.80	69.55	767.11	35.26	6.09	41.35	176.47	34.11	46.50	80.61	396.45						
1.5	398x3063x248	76.31	190.87	267.18	4777.49	35.26	6.09	41.35	653.92	34.47	226.85	261.32	1546.43						
6	382x90x108	30.93	2.27	33.20	78.71	36.53	2.77	39.30	45.84	33.56	2.62	36.18	40.33						
3	763x178x213	34.26	12.63	46.89	461.86	5.33	14.92	50.24	183.02	34.63	12.96	47.59	147.89						
1.5	1526x355x424	0.40	90.92	161.32	3262.15	35.26	105.56	140.82	934.25	33.96	85.79	119.75	764.62						

Table 6.7: Execution Time and Memory Consumption Results from 3 different Flightlines

Chapter 7

Alignment with Hyperspectral Imagery

Chapter 8

Classifications using 3D Prior Models

This talk presents the new features of DASOS, which is an open source software for managing full-waveform LiDAR data and those features are used for detecting dead standing Eucalypt.

The value of dead standing Eucalypt trees from a biodiversity management perspective is large. In Australia, many arboreal mammals and birds that are close to extinct inhabit hollows [5]. Nevertheless, studies predict shortage of hollows in the near future due to tree harvesting and the decades required for a tree to be mature enough to develop a hollow [3] [4]. Dead standing eucalypt trees are more likely to be aged and have hollows, therefore automated detection of them plays a significant role in protecting animals that rely on hollows.

DASOS ($= \delta\alpha\sigma\omega\varsigma$) means forest in Greek and it is an open source software aiming to ease the way of handling FW LiDAR data in forestry [27]. Traditional ways of interpreting FW LiDAR data, suggests extraction of a denser points cloud using Gaussian decomposition [29] [30]. Nevertheless DASOS was influenced by Persson et al, 2005, who used voxelisation to visualise the waveforms [26]. But, DASOS do not only uses voxelisation for visualisations but also for extracting metrics useful in classification. It further normalises the intensities so that equal pulse length exists inside each voxel, making intensities more meaningful. It is further seems that the literature is moving towards voxelisation with the good results obtained at recent publication on tree species classification [33].

The new features of DASOS: New features of DASOS which enables observation at tree level: i.e. distribution of intensities at specific area

The data, provided by RPS Australia East Pty Ltd, were collected in March 2015

from the Riegl (LMS-Q780 or LMS-Q680i?) sensor at an Australian native Forest with eucalyptus. The fieldplots has been provided by (Interprine Group Ltd or Forest Corporation?).

examined with Random Forest

The new features of DASOS are presented and used for generating 3D signatures characterising dead standing trees and a comparison between the discrete and FW LiDAR data is performed to demonstrate the increased survey accuracy obtained with the FW LiDAR.

This paper presents a new feature of DASOS, which is an open source software for managing full-waveform (FW) LiDAR data and that feature is used for detecting dead standing Eucalypt trees in native Australian forests.

The value of dead standing Eucalypt trees from a biodiversity management perspective is large. In Australia, many arboreal mammals and birds, which are close to extinct, inhabit hollows [5]. Nevertheless, studies predict shortage of hollows in the near future due to tree harvesting and the decades required for a tree to develop a hollow [3] [4]. Dead standing eucalypt trees are more likely to be aged and have hollows, therefore automated detection of them plays a significant role in protecting animals that rely on hollows.

The LiDAR data used for this project are provided by RPS Australia East Pty Ltd and they were collected in March 2015 using the Riegl (LMS-Q780 or LMS-Q680i?) sensor. The Riegl LMS-Q??? is a native full-waveform sensor and the LiDAR point clouds were generated from the waveform instrument data during post processing. In addition, the field plots used for the classifications are provided by (Interprine Group Ltd or Forest Corporation?) and contain around 1000 Eucalypt trees while 10% of them are dead.

The new feature of DASOS calculates forestry metrics within a radius relevant to canopy height and exports all metrics into a single vector for fast interpretation in advanced statistical tools. Traditional ways of interpreting FW LiDAR data, suggests extraction of a denser points cloud [29] [30], but as mentioned before with the Riegl system this is done at post processing. Nevertheless DASOS was influenced by Persson et al, 2005, who used voxelisation to visualise the waveforms [26], but DASOS also uses it for generating metrics. It further normalises the intensities so that equal pulse length exists inside each voxel, making intensities more meaningful. Further, recent publication on tree species classification showed that voxelisation could confer good results while interpreting FW LiDAR data [33].

Previous work on dead standing trees detection, suggests single tree segmentation before dead trees identification [69] [70] but in case of Eucalypt trees single tree de-

tection is a challenge on its own due to their irregular structure and multiple trunk splits.

In this project, the new feature of DASOS is used for generating 3D signatures characterising dead standing Eucalypt trees and a comparison between the LiDAR point cloud and FW LiDAR data is performed using Random Forest to demonstrate the increased survey accuracy obtained with voxelisation.

Chapter 9

Comparison with Discrete Data

Furthermore, DASOS allows the user to choose whether the waveform samples or the discrete returns are inserted into the 3D density volume. Each sample or each return has a hit point and an intensity value. So, in both case the space is divided into 3D voxels and the intensity of each return or sample is inserted into the voxel it lies inside.

In general the results of discrete returns contain less information compared to the results from the FW LiDAR, even though the FW LiDAR contain information from about half of the emitted pulses (Section 3). As shown on the 1st example of table 3 the polygon mesh generated from the FW LiDAR contains more details comparing to the one created from the discrete LiDAR. The forest on the top is more detailed, the warehouses in the middle have a clearer shape and the fence on the right lower corner is continuous while in the discrete data it is disconnected and merged with the aliasing.

FW LiDAR polygons, compared to the discrete LiDAR ones, contain more geometry below the outlined surface of the trees. On the one hand this is positive because they include much information about the tree branches but on the other hand the complexity of the objects generated is high. A potential use of the polygon representations is in movie productions: instead of creating a 3D virtual city or forest from scratch, the area of interest can be scanned and then polygonised using our system.

But for efficiency purposes in both animation and rendering, polygonal objects should be closed and their faces should be connected. Hence, in movie productions, polygons generated from the FW LiDAR will require more post-processing in comparison with object generated from the discrete LiDAR.

Example 2 in table 3 shows the differences in the geometry complexity of the discrete and FW polygons using the x-ray shader of Meshlab. The brighter the surface appears the more geometry exists below the top surface. The brightness difference between area 1 and area 2 appears less in the discrete polygon.

Nevertheless, the trees in area 2 are much taller than in area 1, therefore more geometry should have existed in area 2 and sequentially be brighter. But the two areas are only well-distinguished in the FW LiDAR. On average the FW polygon is brighter than the discrete polygon, which implies higher geometry complexity in the FW polygon.

The comparison example 3 is rendered using the Radiance Scaling shader of Meshlab (Vergne et al, 2010). The shader highlights the details of the mesh, making the comparison easier. Not only the FW polygons are more detailed but also holes appear on the discrete polygons. The resolution of the voxels of those examples is 1.7m³ is, the bigger the holes are, while the full-waveform can be polygonised at a resolution of 1m³ without any significant holes. Figure 4 shows an example of rendering the same flightline of examples 3 at the resolution of 1m³ LiDAR data.

The last two examples (4 and 5) compare the side views of small regions. On the one hand the top of the trees are better-shaped in the discrete data. This may occur either because the discrete data contain information from double pulses than the FW data (Section 3) or because the noise threshold of the waveforms is not accurate and the top of the trees appear noisier on the FW LiDAR data. On the other hand more details appear close to the ground on the FW LiDAR data.

*** left during copying :s (and the higher the resolution, using FW)

Chapter 10

Overall Results

Chapter 11

Conclusions

11.1 Contributions

Bibliography

- [1] T. Elmqvist, C. Folke, M. Nyström, G. Peterson, J. Bengtsson, B. Walker, and J. Norberg, “Response diversity, ecosystem change, and resilience,” *Frontiers in Ecology and the Environment*, vol. 1, no. 9, pp. 488–494, 2003.
- [2] D. U. Hooper, F. S. Chapin Iii, J. J. Ewel, A. Hector, P. Inchausti, S. Lavorel, and B. Schmid, “Effects of biodiversity on ecosystem functioning: a consensus of current knowledge,” *Ecological monographs*, vol. 75, no. 1, pp. 3–35, 2005.
- [3] D. B. Lindenmayer and J. T. Wood, “Long-term patterns in the decay, collapse, and abundance of trees with hollows in the mountain ash (eucalyptus regnans) forests of victoria, southeastern australia,” *Canadian Journal of Forest Research*, vol. 40, no. 1, pp. 48–54, 2010.
- [4] R. L. Goldingay, “Characteristics of tree hollows used by australian birds and bats,” *Wildlife Research*, vol. 36, no. 5, pp. 394–409, 2009.
- [5] P. Gibbons and D. Lindenmayer, *Tree Hollows and Wildlife Conservation in Australia*. CSIRO Publishing, 2002.
- [6] “Animal pests: Poss.”
- [7] D. H. DeHayes, P. G. Schaberg, G. J. Hawley, and G. R. Strimbeck, “Acid rain impacts on calcium nutrition and forest health alteration of membrane-associated calcium leads to membrane destabilization and foliar injury in red spruce,” *Bio-Science*, vol. 49, no. 10, pp. 789–800, 1999.
- [8] J. Holmgren, “Prediction of tree height, basal area and stem volume in forest stands using airborne laser scanningce,” *Scandinavian Journal of Forest Research*, vol. 19, no. 6, pp. 543–553, 2004.
- [9] S. G. Aracil and R. B. A. Herries, D.L, “Evaluation of an additional lidar metric in forest inventory,” *Proceedings of Silvilaser*, 2015.

- [10] M. J. Harper, M. A. McCarthy, R. Van Der Ree, and J. C. Fox, “Overcoming bias in ground-based surveys of hollow-bearing trees using double-sampling,” *Forest Ecology and Management*, vol. 190, no. 2, pp. 291–300, 2004.
- [11] L. Rayner, M. Ellis, and J. E. Taylor, “Double sampling to assess the accuracy of ground-based surveys of tree hollows in eucalypt woodlands,” *Forest Ecology and Management*, vol. 36, no. 3, pp. 252–260, 2011.
- [12] R. B. Smith, *Introduction to Hyperspectral Imaging*. MicroImages, 2014.
- [13] W. Wanger, A. Ullrich, T. Melzer, C. Briese, and K. Kraus, “From single-pulse to ful-waveform airborne laser scanners,” *ISPRS Journal of Photogrammetry and Remote Sensing*, vol. 60, pp. 100–112, 2004.
- [14] A. Wehr and U. Lohr, “Airborne laser scanning - an introduction and overview,” *ISPRS Journal of Photogrammetry and Remote Sensing*, vol. 54, pp. 68–82, 1999.
- [15] C. Mallet and F. Bretar, “Full-waveform topographic lidar: State-of-the-art,” *ISPRS Journal of Photogrammetry and Remote Sensing*, vol. 64, pp. 1–16, 2009.
- [16] K. Anderson, S. Hancock, M. Disney, and K. Gaston, “Is waveform worth it? a comparison of lidar approaches for vegetation and landscape characterization,” *Remote Sensing in Ecology and Conservation*, 2015.
- [17] A. Chauve, C. Mallet, F. Bretar, S. Durrieu, M. Deseilligny, and W. Puech, “Processing full-waveform lidar data: Modelling raw signals,” *International Archives of Photogrammetry, Remote Sensing and Spatial Information Sciences*, 2007.
- [18] *LAS Specification version 1.3-R1*. Bethesda, Maryland: American Society for Photogrammetry and Remote Sensing, 2010.
- [19] M. Warren, *Full Waveform Upgrade*. NERC ARSF wiki, 2012.
- [20] M. J. Sumnall, R. A. Hill, and S. A. Hinsley, “Comparison of small-footprint discrete return and full waveform airborne lidar data for estimating multiple forest variables,” *Remote Sensing of Environment*, vol. 173, pp. 214–223, 2016.
- [21] K. H. R. A. . Z. A. Lehner, H., “Consideration of laser pulse fluctuations and automatic gain control in radiometric calibration of airborne laser scanning data.,” *Proceedings of 6th ISPRS Student Consortium and WG VI/5 Summer School*, 2011.
- [22] I. Korpela, H. O. Ørka, H. V. Hyppä, J., and T. Tokola, “Range and agc normalization in airborne discrete-return lidar intensity data for forest canopies,” vol. 65, no. 4, pp. 369–379, 2010.

- [23] M. Isenburg, *LAStools - efficient tools for LiDAR processing*. rapidlasso.
- [24] M. Warren, B. Taylor, M. Grant, and J. D. Shutler, “Data processing of remorely sensed airborne hyperspectral data using the airborne processing library (apl),” *ScienceDirect, Computers and Geosciences*, vol. 64, 2014.
- [25] M. Isenburg, “Pulsewaves: An open, vendor-neutral, stand-alone, las-compatible full waveform lidar standard.,” 2012.
- [26] A. Persson, U. Soderman, J. Topel, and S. Ahlberg, *Visualisation and Analysis of full-waveform airborne laser scanner data*. V/3 Workshop, Laser scanning 2005, 2005.
- [27] M. Miltiadou, M. A. Warren, M. Grant, and M. Brown, “Alignment of hyper-spectral imagery and full-waveform lidar data for visualisation and classification purposes,” *The International Archives of Photogrammetry, Remote Sensing and Spatial Information Sciences*, vol. 40, no. 7, p. 1257, 2015.
- [28] W. Wanger, A. Ullrich, V. Ducic, T. Maizer, and N. Studnicka, “Gaussian decompositions and calibration of a novel small-footprint full-waveform digitising airborne laser scanner,” *ISPRS Journal of Photogrammetry and Remote Sensing*, vol. 60, pp. 100–112, 2006.
- [29] A. Neuenschwander, L. Magruder, and M. Tyler, “Landcover classification of small-footprint full-waveform lidar data,” *Jounal of Applied Remote Sensing*, vol. 3, no. 1, pp. 033544–033544.
- [30] J. Reitberger, P. Krzystek, and U. Stilla, “Analysis of full waveform LiDAR data for tree species classification,” *International Journal of Remote Sensing*, vol. 29, no. 5, pp. 1407–1431, 2008.
- [31] A. Chauve, F. Bretar, S. Durrieu, M. Pierrot-Deseilligny, and W. Puech, “Fullanalyse: A research tool for handling, processing and analysing full-waveform lidar data,” *IEEE International Geoscience and Remote Sensing Symposium*, 2009.
- [32] P. Bunting, J. Armston, D. Clewley, and R. M. Lucas, “Sorted pulse data (spd) library—part ii: A processing framework for lidar data from pulsed laser systems in terrestrial environments,” *Computers & Geosciences*, vol. 56, pp. 207–215, 2013.
- [33] L. Cao, N. Coops, L. Innes, J. Dai, and H. Ruan, “Tree species classification in subtropical forests using small-footprint full-waveform lidar data,” *International Journal of Applied Earth Observation and Geoinformation*, vol. 49, pp. 39–51, 2016.

- [34] M. Miltiadou, M. Grant, M. Brown, M. Warren, and E. Carolan, “Reconstruction of a 3d polygon representation from full-wavefrom lidar data,” *RSPSoc Annual Conference 2014, New Sensors for a Changing World*, 2014.
- [35] R. Crippen, “Calculating the vegetation index faster,” *Remote Sensing of Environment*, vol. 34, no. 1, pp. 71–73, 1990.
- [36] R. N. Clark, G. A. Swayze, R. Wise, K. E. Livo, T. Hoefen, R. F. Kokaly, and S. J. Sutley, “Usgs digital spectral library splib06a,” *US Geological Survey, Digital Data Series*, vol. 231, 2007.
- [37] P. Hanrahan, “Ray tracing algebraic surfaces,” *ACM SIGGRAPH Computer Graphics*, vol. 17, no. 3., 1983.
- [38] H. Pfister, J. Harderbergh, J. Knittel, H. Lauer, and L. Seiler, “The volumepro real-time ray-casting system,” *Proceedings of the 26th annual conference on Computer graphics and interactive techniques*, pp. 251–260, 1999.
- [39] C. Crassin, F. Neyret, S. Lefebvre, and E. Eisemann, “Gigavoxels: Ray-guided streaming for efficient and detailed voxel rendering,” *Proceedings of the 2009 symposium on Interactive 3D graphics and games*, pp. 15–22, 2009.
- [40] J. F. Blinn, *A Generalization of Algebraic Surface Drawing*, vol. 1. ACM Transactions on Graphics (TOG).
- [41] A. Pasko and V. Savchenko, *Blending operations for the functionally based constructive geometry*. 1994.
- [42] W. E. Lorensen and H. E. Cline, “Marching cubes: A high resolution 3d surface construction algorithm,” *ACM Siggraph Computer Graphics*, vol. 21, pp. 163–169, 1987.
- [43] M. Levoy, “Volume rendering: Display of surfaces from volume data,” *IEEE Computer Graphics and Applications*, vol. 8, no. 3, pp. 29–37, 1998.
- [44] M. Hadwiger, J. Beyer, W. K. Jeong, and H. Pfister, “Interactive volume exploration of petascale microscopy data streams using visualizatin-driven virtual memory approach,” *IEEE Transactions on Visualisation and Computer Graphics*, 2012.
- [45] S. Laine and T. Karras, “Efficient sparse voxel octrees,” *Visualization and Computer Graphics, IEEE Transactions*, vol. 17, no. 8, pp. 1048–1059, 2011.

- [46] B. Rodrigues de Araujo and J. A. Pires Jorge, *Adaptive polygonization of implicit surfaces*, vol. 29. Science Direct, Computer and Graphics, 2005.
- [47] E. Hartmann, “A marching method for the triangulation of surfaces,” *The Visual computer* 14, no. 14, no. 3, pp. 95–108, 1998.
- [48] C. D. Hansen and P. Hinken, “Massively parallel isosurface extraction,” *Proceedings of the 3rd conference on Visualization '92*, pp. 77–83, 1992.
- [49] C. Galbraith, P. MacMurchy, and B. Wyvill, *BlobTree Trees*. IEEE Computer Graphics International, 2004.
- [50] H. Sutter and A. Alexandrescu, *C++ Coding Standards: 101 Rules, Guidelines, and Best Practices*. United States: Addison-Wesley, 2004.
- [51] J. Wilhelms and A. Van Gelder, “Octrees for faster isosurface generation,” vol. 24, no. 5, 1990.
- [52] . W. J. Schaefer, S., “Dual marching cubes: Primal contouring of dual grids,” *Computer Graphics Forum*, vol. 24, no. 2, 2005.
- [53] J. Wilhelms and A. Van Gelder, “Octrees for faster isosurface generation,” *ACM Transactions on Graphics (TOG)*, vol. 11, no. 3, pp. 201–227, 1992.
- [54] S. F. Gibson, “Constrained elastic surface nets: Generating smooth surfaces from binary segmented data,” *International Conference on Medical Image Computing and Computer-Assisted Intervention*, pp. 888–898, 1998.
- [55] B. Chazelle and L. J. Guibas, “Fractional cascading: I. a data structuring technique.,” *Algorithmica*.
- [56] K. Museth, “Vdb: High-resolution sparse volumes with dynamic topology,” *ACM Transactions on Graphics (TOG)*, vol. 32, no. 3, p. 27, 2013.
- [57] M. S. Warren and J. K. Salmon, “A parallel hashed oct-tree n-body algorithm,” *In Proceedings of the 1993 ACM/IEEE conference on Supercomputing*, pp. 12–21, 1993.
- [58] M. Nießner, M. Zollhöfer, S. Izadi, and M. Stamminger, “Real-time 3d reconstruction at scale using voxel hashing,” *ACM Transactions on Graphics (TOG)*, vol. 32, no. 2, p. 169, 2013.
- [59] F. C. Crow, “Summed-area tables for texture mapping,” *ACM Computer Graphics*, vol. 18, no. 3, pp. 207–212, 1984.

- [60] S. Hanan, “Neighbor finding in images represented by octrees,” *Computer Vision, Graphics, and Image Processing*, vol. 46, no. 3, pp. 367–386, 1989.
- [61] G. Schrack, “Finding neighbors of equal size linear quadtrees and octrees in constant time,” *CVGIP: Image Understanding*, vol. 55, no. 3, pp. 221–230, 1992.
- [62] R. Lohner, “Robust, vectorized search algorithms for interpolation on unstructured grids,” *Journal of Computational Physics*, vol. 118, no. 2, pp. 380–387, 1995.
- [63] R. Castro, T. Lewiner, H. Lopes, G. Tavares, and A. Bordignon, “Statistical optimisation of octree searches,” *Computer Graphics Forum*, vol. 27, no. 6, pp. 1557–1566, 2008.
- [64] M. L. Clark, D. A. Roberts, J. J. Ewel, and D. B. Clark, “Estimation of tropical rain forest aboveground biomass with small-footprint lidar and hyperspectral sensors,” *ScienceDirect, Remote Sensing of Environment*, vol. 115.
- [65] J. E. Anderson, L. C. Plourde, M. E. Martin, B. H. Braswell, M. L. Smith, R. O. Dubayah, M. A. H. Dubayah, and J. B. Blair, “Integrating waveform lidar with hyperspectral imagery for inventory of a northern temperate forest,” *Remote Sensing of Environment*, vol. 112, no. 4, pp. 1856–1870, 2008.
- [66] H. Buddenbaum, S. Seeling, and J. Hill, “Fusion of full-waveform lidar and imaging spectroscopy remote sensing data for the characterization of forest stands,” *International Journal of Remote Sensing*, vol. 32, no. 13, pp. 4511–4524, 2013.
- [67] J. Heinzel and B. Koch, “Investigating multiple data sources for tree species classification in temperate forest and use for single tree delineation,” *International Journal of Applied Earth Observation and Geoinformation*, vol. 18, pp. 101–110, 2012.
- [68] R. G. Congalton, “A review of assessing the accuracy of classifications of remotely sensed data,” *Remote Sensing of Environment*, vol. 37, no. 1.
- [69] W. Yao, P. Krzystek, and M. Heurich, “Identifying standing dead trees in forest areas based on 3d single tree detection from full-waveform lidar data,” *ISPRS Annals of the Photogrammetry, Remote Sensing and Spatial Information Sciences*, vol. I-7, pp. 359–364, 2012.
- [70] P. Polewski, W. Yao, M. Heurich, P. Krzystek, and U. Stilla, “Active learning approach to detecting standing dead trees from als point clouds combined with aerial infrared imagery,” *Proceedings of the IEEE Conference on Computer Vision and Pattern Recognition Workshops*, pp. 10–18, 2015.

Chapter 12

Appendices

12.1 Birds and Mammals Catalogue

12.1.0.1 Introduction

12.1.0.2 Australian arboreal Mammals

12.1.0.3 Australian Birds

The Forestry Corporation, Australia, provided a list of bird species that rely on hollows. But species are not limited to that list and more species rely uses hollows for shelters.

The provided list of the birds is divided into three groups:

1. Categorised as threatened species according to the Environment Protection and Biodiversity Conservation Act, 1999

Corella Eastern Rosella Superb Parrot Barking Owl Masked Owl

2. All the above species are included to the Action Plan for Australian Birds, 2000, as well as the following once:

Powerful Owl Sooty Owl

3. The rest:

Kookaburra Sulphur Crested Cockatoo Crimson Rosella Rainbow Lorikeet Musk Lorikeet Little Lorikeet Red-winged Parrot Cockatiel Australian Ringneck (Parrot) Red-rumped Parrot Powerful Owl Sooty Owl Barn Owl White-throated Treecreeper

12.1.0.4 Web-links of Photos

Mammals · Brush-tailed Possum - protected wildlife (Hollow: <http://www.cavershamwildlife.com.au/comm-brushtail-possum/>) (<http://www.rymich.com/girraween/photos/animals/mammals/possums/trichosurus-brushtail-possum.html>) .

Birds · Kookaburra (<http://tenrandomfacts.com/blue-winged-kookaburra/>) .

Sulphur Crested Cockatoo (<http://aussiegal7.deviantart.com/art/Sulphur-Crested-Cockatoo-08-1000x750>) .

- Corella (<http://www.theparrotplace.co.nz/all-about-parrots/long-billed-corella/>)
- Crimson Rosella (http://25.media.tumblr.com/tumblr_m3mo89c40r1r4t9h1o1_1280.jpg)
- Eastern Rosella (http://2.bp.blogspot.com/-pYxw51WjSOY/UB-LEFgd2KI/AAAAAAAAGw/9z60PUWE6TE/s1600/_GJS6601-as-Smart-Object-1.jpg)
- Galah (<https://www.pinterest.com/pin/537546905498955709/>)
- Rainbow Lorikeet (https://www.reddit.com/r/pics/comments/328fvc/a_rainbow lorikeet_found_in_coastal_regions/)
- Musk Lorikeet (http://www.rymich.com/girraween/photos/animals/birds/medium/glossopsitta concinna/glossopsitta_concinna_001.jpg)
- Little Lorikeet (<http://www.pbase.com/sjmurray/psittacidae>)
- Red-winged Parrot (<https://www.pinterest.com/pin/395894623469889727/>)
- Superb Parrot (<http://www.davidkphotography.com/?showimage=637>)
- Cockatiel (<http://up.parsipet.ir/uploads/Cockatiels-for-sale.jpg>)
- Australian Ringneck (Parrot) (<http://ontheroadmagazine.com.au/wp-content/uploads/2015/09/Twenty-eight-parrot-2.jpg>)
- Red-rumped Parrot (<http://parrotfacts.net/wp-content/uploads/Red-Rumped-Parrot-on-a-.jpg>)
- Powerful Owl (http://farm1.staticflickr.com/219/495796536_f78dac04c1.jpg)
- Sooty Owl (hollow: http://www.mariewinn.com/marieblog/uploaded_images/screech2-738532.jpg) (http://www.owlpages.com/owls/species/images/greater_sooty_owl_richard_jackson-1.jpg)
- Barking Owl (<http://www.pcpimages.com/Nature-and-Wildlife-Birds/i-7JKSTp5/1/L/owl%20%281%20of%201%29-L.jpg>)
- Masked Owl (http://www.survival.org.au/images/birds/masked_owl_2_600.jpg)
- Barn Owl (Hollow: http://www.barnowltrust.org.uk/wp-content/uploads/Barn_Owl_hollow_tree-wallpaper.jpg) (https://upload.wikimedia.org/wikipedia/commons/c/c6/Tyto_alba_-British_Wildlife_Centre,_Surrey,_England-8a_%281%29.jpg)
- White-throated Treecreeper (<http://www.birdlifemelbourne.org.au/bird-lists/47-Treecreepers/White-throated-Treecreeper/White-throated%20Treecreeper%2020JB.jpg>) (hollow: <https://geoffpark.files.wordpress.com/2011/09/female-white-throated-treecreeper-1.jpg>)
- Hollow Owl: http://www.mariewinn.com/marieblog/uploaded_images/screech2-738532.jpg